



Full Length Article

CFD analysis of combustion and emission characteristics of primary reference fuels: from transient Diesel spray to heavy-duty engine

Qiyang Zhou^{a,b,*}, Tommaso Lucchini^b, Gianluca D'Errico^b, Ricardo Novella^c,
Jose María García-Oliver^c, Xingcai Lu^a

^a Key Lab. for Power Machinery and Engineering of M. O. E, Shanghai Jiao Tong University, China

^b Department of Energy, Politecnico di Milano, Italy

^c CMT Motores Térmicos – Universitat Politècnica de València, Spain



ARTICLE INFO

Keywords:

Computational fluid dynamics
Diesel combustion modeling
Soot modeling
Tabulated flamelet progress variable
Primary reference fuels

ABSTRACT

The pre-blending of low- and high-reactivity fuels for a single direct injection system has been proven to be an effective way to control the reactivity of mixtures in compression ignition engines, having the potential to simultaneously reduce fuel consumption and pollutant emissions. However, there is not much knowledge about the complex physical–chemical phenomena in the turbulent sprays with fuels having widely different auto-ignition qualities, although this information is critical for the design and development of cleaner combustion systems based on this concept. For this reason, a computational analysis of ignition behavior, flame structure, and soot production for reacting sprays with five primary reference fuels (PRFs), from PRF0 (n–heptane) to PRF80 (20% n–heptane, 80% iso-octane) with 20% increment in iso-octane mass fraction, was first performed using the Tabulated Flamelet Progress Variable (TFPV) approach based on the tabulation of diffusion flamelets for different scalar dissipation rates. The temporal and spatial features of the flame structure and soot formation for different fuels were investigated with the so-called intensity-axial distance-time (IXT) plots. Then, ten PRFs, from RRF0 to PRF90 with 10% increment in iso-octane mass fraction, were investigated and compared in a heavy-duty Diesel engine operating at the conventional high-temperature, short-ignition delay (HTSID) condition. The injection timing was altered from -5 to -13 ° ATDC to optimize the combustion phase and engine performance for different fuels. The results showed that PRF70 exhibited the best performance at the tested condition, which reduced the soot mass to 5% of the baseline value without sacrificing fuel efficiency.

1. Introduction

Compression ignition (CI) engines will continue to play a dominant role in heavy-duty applications due to their high fuel efficiency and power density advantages. The primary development of today's CI engine aims to meet the strict legislative regulations for nitrogen oxide (NO_x) and soot without using costly and complex after-treatment systems, which has challenged the efforts of many researchers over the past decades [1–4]. A dual fuel engine combustion technology known as reactivity controlled compression ignition (RCCI) has been widely proven to be a promising concept to reduce pollutant emissions while keeping competitive or even favorable engine efficiency compared to conventional CI engines [4–6]. It is implemented by an in-cylinder fuel blending with at least two fuels with different reactivity: the low reactivity fuel is injected into the intake port to create a well-mixed charge

while the high reactivity fuel is directly injected into the cylinder before ignition of the premixed fuel [4,7], which, however, results in two injection systems, two refueling actions, higher costs and worse packaging.

An attractive alternative to overcome the aforementioned issues is using a pre-blended fuel tailoring the physical and chemical properties injected through a single direct injection system. Extensive studies were conducted to explore the potential of such technology: In [8], experiments using Diesel, gasoline-Diesel blends of 20% and 40% gasoline mass fraction, showed that the lower auto-ignition quality of gasoline could improve fuel–air mixing before the onset of combustion and significantly suppress the soot formation. In [9], five gasoline-Diesel blends with gasoline volume ratio varying from 20% to 60% were tested, and the results confirmed that a high gasoline fraction was effective in reducing the nitrogen oxides (NO_x) and smoke emissions

* Corresponding author at: Key Lab. for Power Machinery and Engineering of M. O. E, Shanghai Jiao Tong University, China.

E-mail address: qiyang.zhou@polimi.it (Q. Zhou).

simultaneously at the optimum combustion phase without giving significant penalty of fuel consumption. A novel concept, termed as Gasoline Compression Ignition (GCI), was also put forward by Kalghatgi in [10], where fuels in the gasoline auto-ignition quality range are used in CI engines to increase ignition and mixing times, mitigating emissions typically generated in conventional Diesel engines [11–13]. There have been many studies on seeking the ideal fuel research octane number (RON) range for GCI engine [14–16]. In [14], four gasoline fuels (RON = 72, 78, 84, 91) were tested in a single-cylinder light-duty engine with a compression ratio of 16, and it was found that the optimum fuel should have a RON span from 75 to 85. In [15], an experimental study on a heavy-duty engine suggested the optimum RON for GCI to be in the range of 70. Primary reference fuel (PRF), a bi-component mixture of n-heptane and iso-octane, is widely used to study the effects of fuel auto-ignition quality on engine combustion and emission characteristics due to its simplicity and flexibility of adjusting octane number from Diesel-like to gasoline-like fuels compared to the more complex surrogate fuels (e.g. TRF) [16]. The studies in [17,18] showed that the combustion and emission characteristics of actual fuel could be accurately reproduced by PRF. In [16], four PRFs (PRF60, PRF70, PRF80, PRF90) were used to enable a flexible adjustment of fuel RON for the GCI engine operation, and the obtained results further underlined the role of fuel reactivity in CI engine combustion and pollutant formation processes.

However, most of the studies were conducted either in the Diesel-like or the gasoline-like fuel ranges, while a more comprehensive and in-depth understanding of how fuel RON affects the combustion and emission formation processes is becoming essential for the continuous development and successful commercial implementation of the pre-blended dual-fuel technology. This has been at the forefront of engine research and requires not only experimental efforts in optically accessible rigs [19,20], but also predictive and robust computational fluid dynamics tools to gain more insight into the complex multi-scale physics and chemistry of turbulent spray flames with fuels having widely different reactivity properties. In particular, the combustion model must be able to capture subtle influences of fuel composition on combustion and pollutants formation processes. Such demand has attracted a lot of attentions on the development of combustion model based on detailed chemistry and turbulence-chemistry interaction in the last decades, including representative interactive flamelet (RIF)[21]22, transport probability density function (TPDF)[23]. These approaches are flexible with respect to fuels, mechanisms, and operating conditions, but with a consequence of high computational costs. A possible alternative to reduce CPU time can be represented by tabulated kinetics, which includes realistic chemistry by means of pre-tabulated solutions based on assumed flame structures [24–27] and parameterizes the thermochemical evolution in the composition and temperature spaces by a reduced set of variables [28]. Regarding the turbulent spray modeling, a set of models falling into such technique were compared in [29,30], including tabulated well-mixed model (TWM), tabulated representative flamelet interactive model (TRIF), tabulated presumed PDF approach (TPPDF), and the tabulated flamelet progress variable approach (TFPV). The results proved that the TFPV model based on approximated diffusion flamelets [31–33] performs better in the description of spray flames due to the consideration of turbulence-chemistry interaction and local distribution of scalar dissipation rate, which has also been comprehensively validated by authors in the modeling of spray flames with single and double injections [34,35], as well as light- and heavy-duty Diesel engines [29,36,37].

The purpose of this work is to comprehensively investigate the combustion and emission characteristics of fuels having widely different auto-ignition qualities in both transient high-pressure spray flames and a heavy-duty Diesel engine. Non-reacting spray in a high-pressure high-temperature vessel using specifications from the Engine Combustion Network (ECN) [38] was first simulated to validate the accuracy of the computational setups. The computed ignition delays and lift-off lengths were then compared with experiments [39,40] to evaluate the capability

of the TFPV approach in capturing the effects of fuel reactivity. Following the successful validation of numerical models, the ignition behavior, the temporal and spatial characteristics of the flame structure, and soot formation were thoroughly studied and compared for five PRFs, from PRF0 (n-heptane) to PRF80 (20% n-heptane, 80% iso-octane). Then, the engine experimental data in [41], including pressure, apparent heat release rate, soot and NO_x emissions, was used to validate the chosen combustion and emission models. Ten PRFs, from RRF0 to PRF90 with 10% increment in iso-octane mass fraction, were tested at a high-temperature, short-ignition delay operating condition. Different start of injection (SOI) ranging from −5 to −13 ° ATDC was tested to maintain an optimal combustion phase for different fuels, especially avoid too delayed auto-ignition when lowering the fuel reactivity. The engine efficiency, NO_x and soot emissions were investigated and compared to comprehensively understand the effects of fuel auto-ignition quality and find the optimum fuel for CI engines.

2. Combustion and emission models

2.1. Tabulated flamelet progress variable

The main purpose of the TFPV model is to provide a realistic description of turbulent diffusion flames with an affordable computational cost. Owing to the use of progress variable and scalar dissipation rate, it takes into account turbulence-chemistry interaction, sub-grid mixing, premixed flame propagation, and gives correct predictions of extinction, re-ignition and flame stabilization processes. The operation of the TFPV model is generally divided into two parts: the generation of offline TFPV table and the coupling between CFD solver and look-up table.

2.1.1. TFPV table

Fig. 1 summarizes the generation of TFPV table. A range of unburned temperature, pressure, stoichiometric scalar dissipation rate are provided for the unsteady diffusion flame calculations in the mixture fraction space [42,32,33] by means of solving approximated flamelet equations for the progress variable and the enthalpy, which are formulated based on unity Lewis number assumption [21]:

$$\rho \frac{\partial C}{\partial t} = \rho \frac{\chi_z}{2} \frac{\partial^2 C}{\partial Z^2} + \dot{C} \quad (1)$$

$$\rho \frac{\partial h}{\partial t} = \rho \frac{\chi_z}{2} \frac{\partial^2 h}{\partial Z^2} + \frac{\partial p}{\partial t} \quad (2)$$

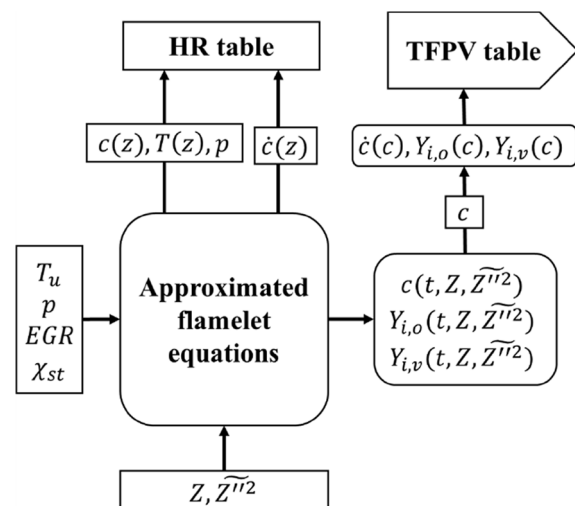


Fig. 1. Generation of TFPV chemistry table.

where C is the progress variable, defined as the heat released by combustion [42], and its source term \dot{C} is taken from the chemistry table generated from the constant pressure homogeneous reactor calculations [29,36]. The function form of the dependence of scalar dissipation rate χ_z on mixture fraction Z in the flamelet is typically represented by an error function profile [43]:

$$\chi = \chi_{st} \frac{\exp\left(-2|\operatorname{erfc}^{-1}(2Z)|^2\right)}{\exp\left(-2|\operatorname{erfc}^{-1}(2Z_{st})|^2\right)} \quad (3)$$

At each time step, the progress variable $C(Z, t)$ and the chemical compositions in terms of the virtual species $Y_{i,v}(Z, t)$ ($N_2, O_2, \text{fuel}, CO_2, CO, H_2O, H_2$), whose mass fractions are computed to preserve the main thermochemical properties of the full set of species involved in the specified mechanism [30,44], can be estimated for the prescribed values of Z . The mixture fraction variance \widetilde{Z}''^2 is computed from user-specified mixture fraction segregation factors:

$$S_z = \frac{\widetilde{Z}''^2}{Z(1-Z)} \quad (4)$$

The results of flamelet calculations are then processed to account for sub-grid mixing by virtue of assuming β -PDF distribution for both progress variable and chemical compositions:

$$\widetilde{Y}_i(Z, \widetilde{Z}''^2) = \int_0^1 Y_i(Z) \beta(Z, \widetilde{Z}''^2) dZ \quad (5)$$

$$\widetilde{C}(Z, \widetilde{Z}''^2) = \int_0^1 C(Z) \beta(Z, \widetilde{Z}''^2) dZ \quad (6)$$

At the end of any diffusion flame calculation, for all values of Z and \widetilde{Z}''^2 , the progress variable is normalized with respect to the min-max values encountered in each flame calculation, and its reaction rate is estimated according to:

$$\dot{c}_i = \frac{c_{i+1} - c_i}{t_{i+1} - t_i} \quad (7)$$

where the c is the normalized progress variable. Assuming δ -PDF distribution for chemical species in progress variable space, the computed data are then interpolated for the discrete values of c to generate the chemistry table.

2.1.2. CFD solver

Fig. 2 presents the operation principle of TFPV combustion model, illustrating the mutual interaction between CFD solver and lookup table. In the CFD domain, additional transport equations need to be solved for mixture fraction Z , mixture fraction variance \widetilde{Z}''^2 , progress variable C , unburned gas enthalpy h_u , and stoichiometric scalar dissipation rate χ_{st} .

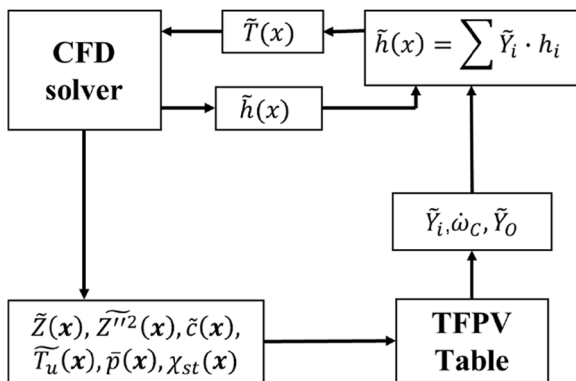


Fig. 2. Operation of combustion models based on tabulated kinetics.

The spray evaporation effects \dot{S}_Z are considered in the mixture fraction equation:

$$\frac{\partial \bar{\rho} \widetilde{Z}}{\partial t} + \nabla \cdot \left(\bar{\rho} \widetilde{U} \widetilde{Z} \right) - \nabla \cdot \left(\frac{\bar{\mu}_t}{Sc_t} \nabla \widetilde{Z} \right) = \dot{S}_Z \quad (8)$$

Assuming the sub-grid distribution of mixture fraction can be represented by β -PDF, its variance equation needs to be solved:

$$\frac{\partial \bar{\rho} \widetilde{Z}''^2}{\partial t} + \nabla \cdot \left(\bar{\rho} \widetilde{U} \widetilde{Z}''^2 \right) - \nabla \cdot \left(\frac{\bar{\mu}_t}{Sc_t} \nabla \widetilde{Z}''^2 \right) = 2 \frac{\bar{\mu}_t}{Sc_t} |\nabla \widetilde{Z}|^2 - \bar{\rho} \widetilde{\chi} \quad (9)$$

where $\widetilde{\chi}$ is the average scalar dissipation rate, being a function of turbulent time scale and mixture fraction variance:

$$\widetilde{\chi} = C_{\chi} \frac{\bar{\epsilon}}{k} \widetilde{Z}''^2 \quad (10)$$

The transport equations of the progress variable and the unburned gas enthalpy h_u that is then used to estimate the unburned gas temperature T_u are solved as following:

$$\frac{\partial \bar{\rho} \widetilde{C}}{\partial t} + \nabla \cdot \left(\bar{\rho} \widetilde{U} \widetilde{C} \right) - \nabla \cdot \left(\frac{\bar{\mu}_t}{Sc_t} \nabla \widetilde{C} \right) = \bar{\rho} \dot{C} \quad (11)$$

$$\frac{\partial \bar{\rho} \widetilde{h}_u}{\partial t} + \nabla \cdot \left(\bar{\rho} \widetilde{U} \widetilde{h}_u \right) - \nabla \cdot \left(\bar{\alpha}_t \nabla \widetilde{h}_u \right) = \dot{Q}_s + \frac{\bar{p}}{\rho_u} \frac{D\bar{p}}{Dt} \quad (12)$$

where the source term in the progress variable transport equation (Eq. (11)) is taken from the TFPV table. In Eq. (12), α_t is the turbulent thermal diffusivity and ρ_u is the density of unburned gases which is computed from local cell pressure, chemical compositions at $c = 0$ and T_u . \dot{Q}_s is the source term related to spray evaporation. The Hellstrom formulation [21] is used to compute the stoichiometric scalar dissipation rate χ_{st} :

$$\chi_{st} = \frac{\widetilde{\chi}}{\int_0^1 \frac{f_{erfc}(Z)}{f_{erfc}(Z_{st})} \widetilde{P}(Z) dZ} \quad (13)$$

where f_{erfc} has an erfc-profile and $\widetilde{P}(Z)$ is a β -PDF function, whose parameters depend on mixture fraction and mixture fraction variance. The local cell values of $Z, \widetilde{Z}''^2, C, p, T_u$ and χ_{st} are then used to access the TFPV table, which provides the chemical compositions and the progress variable reaction rate to the CFD solver by performing an inverse, distance weighted interpolation. It should be highlighted that the progress variable C generated from the cool-flame in rich mixtures is very high, and it could be transported to the lean or stoichiometric region by diffusion and convection. Such high values of C could ignite the lean or stoichiometric mixtures almost instantly, leading to a very advanced auto-ignition event. To overcome this, reaction rates are set to zero in the regions where two-stage ignition does not happen (approximately $\phi > 3$).

2.2. NO_x emissions

Concerning the NO_x prediction, a tabulated approach on the basis of homogeneous reactor was developed and an additional transport equation was solved:

$$\frac{\partial \bar{\rho} \widetilde{Y}_{NO_x}}{\partial t} + \nabla \cdot \left(\bar{\rho} \widetilde{U} \widetilde{Y}_{NO_x} \right) - \nabla \cdot \left(\frac{\bar{\mu}_t}{Sc_t} \nabla \widetilde{Y}_{NO_x} \right) = \dot{\omega}_{NO_x} \quad (14)$$

where the $\dot{\omega}_{NO_x}$ is the formation rate of NO_x, and Y_{NO_x} is defined as:

$$Y_{NO_x} = Y_{NO} + Y_{NO_2} + Y_{N_2O} + Y_{N_2O_2} \quad (15)$$

The homogeneous reactor calculations are performed until Y_{NO_x} reaches equilibrium value, which happens much later than combustion since the time-scales of NO_x formation are longer than those governing fuel oxidation (Fig. 3). To this end, the NO_x formation rate cannot be expressed only as a function of the main thermodynamic conditions and progress variable and a new progress variable is necessary to be introduced:

$$c_{NO_x} = \frac{Y_{NO_x}}{Y_{eq,NO_x}} \quad (16)$$

where Y_{eq,NO_x} is the maximum Y_{NO_x} value evaluated at the end of reactor calculations. It is stored in the table as function of the initial thermodynamic conditions (p, T_u, Z, EGR (Exhaust gas recirculation)). The normalized progress variable reaction rate \dot{c}_{NO_x} can be evaluated as function of:

1. normalized combustion progress variable:

$$\dot{c}_{NO_x,1} = \frac{c_{NO_x}(c_{i+1}) - c_{NO_x}(c_i)}{t(c_{i+1}) - t(c_i)} \quad (17)$$

2. normalized NO_x progress variable:

$$\dot{c}_{NO_x,2} = \frac{c_{NO_x,i+1} - c_{NO_x,i}}{t(c_{NO_x,i+1}) - t(c_{NO_x,i})} \quad (18)$$

The source term of Eq. (14) is then computed as:

$$\dot{\omega}_{NO_x} = \rho Y_{eq,NO_x} \dot{c}_{NO_x,1} \quad \text{if } c < \bar{c} \quad (19)$$

$$\dot{\omega}_{NO_x} = \rho Y_{eq,NO_x} \dot{c}_{NO_x,2} \quad \text{if } c \geq \bar{c} \quad (20)$$

where \bar{c} is a threshold value which is set to 0.99. The sensitivity of the computed NO_x values from \bar{c} is low, provided that a sufficiently high value is selected ($\bar{c} > 0.5$). The use of two normalized progress variables makes it possible to distinguish prompt and thermal NO_x by associating the NO_x formation with ignition progress (prompt NO_x) and afterwards (thermal NO_x). Therefore, with such technique, both prompt and thermal NO_x concentrations are possible to be estimated when suitable NO_x kinetic mechanisms are included.

2.3. Soot model

The Leung-Lindstedt-Jones (LLJ) semi-empirical model [45] was

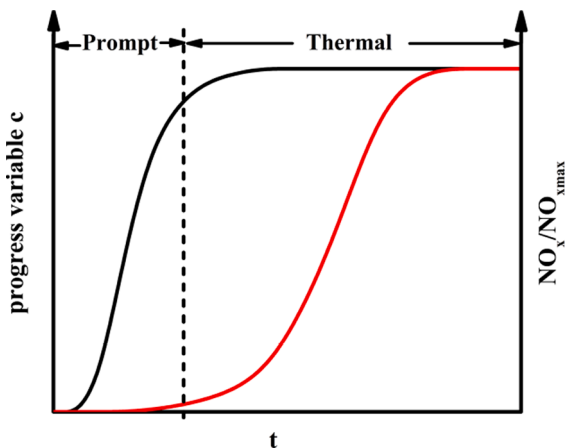


Fig. 3. Evolution in time of normalized progress variable and normalized NO_x for an auto-ignition event in a constant-pressure reactor.

employed to estimate soot emissions. Transport equations for soot particle number density N_p and volume fraction f_v are solved in the CFD domain, with source terms related to nucleation, coagulation, surface growth and oxidation processes as follows:

$$\dot{\omega}_{N_p} = \dot{\omega}_{inc} - \dot{\omega}_{coag} \quad (21)$$

$$\dot{\omega}_{f_v} = \dot{\omega}_{inc} + \dot{\omega}_{grow} - \dot{\omega}_{oxi,O_2} - \dot{\omega}_{oxi,OH} - \dot{\omega}_{oxi,O} \quad (22)$$

Inception and surface growth source term ($\dot{\omega}_{inc}$ and $\dot{\omega}_{grow}$) depend linearly on the soot precursor - acetylene (C_2H_2) concentration, calculated by assuming the following reaction steps:

- Inception: $C_2H_2 \rightarrow 2C(s) + H_2$
- Surface growth: $C_2H_2 + nC(s) \rightarrow (n+2)C(s) + H_2$

The soot surface growth rate is assumed to be proportional to the square root of the specific surface area in the present work, following [45]. In such a way, the reduced reactivity of soot particles over time can be taken into account. Coagulation of soot particles ($\dot{\omega}_{coag}$) presented in the source term of the number density equation is modeled using the normal square dependence. Soot oxidation from O_2, OH and O are considered in the source term of the volume fraction f_v equation.

3. Diesel-like spray combustion vessel

Experiments conducted in the CMT combustion vessel, where the Diesel-like conditions (high temperature and high pressure) can be reached and optical techniques including high-speed Schlieren and time-averaged OH^* chemiluminescence are available [20,46,40], were used for the validation and analysis. The fuels were delivered by a single-hole Spray A injector (# 210675) within the Engine Combustion Network (ECN) [38], an international collaboration among different research laboratories. Different blends of n-heptane and iso-octane were tested and the injection duration was kept at 3.5 ms. Simulations were conducted for five blends (PRF0, PRF20, PRF40, PRF60, PRF80) at the baseline condition using the Lib-ICE code, a set of solvers and libraries for IC engine modeling developed under the OpenFOAM technology [47–49].

Simulations were performed in a 3D mesh, representing the entire domain of the CMT combustion vessel. The cross-section view of the computational mesh is shown in Fig. 4, where the red arrow depicts the injection direction. The mesh structure is similar to what is generally employed in practical IC engine simulations [44,37]: the grid is refined in the vicinity of injector and its resolution progressively decreases when moving downstream of the injector and the combustion vessel walls to reduce the computational time, having about 0.4 million cells with a minimum size of 0.2 mm. The applied turbulence and spray sub-models

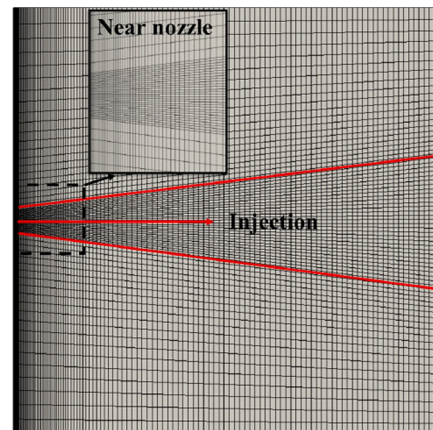


Fig. 4. Cross-section of computational domain.

are summarized in Table 1. For the assessment of the choices of mesh size, turbulence and spray sub-models, a non-reacting case was first considered for PRF0 at baseline Spray A condition. The computed liquid and vapor penetrations are compared with measured data in Fig. 5, where the computed liquid length is obtained by projected liquid volume (PLV) approach [50,51]: a Eulerian liquid volume fraction field is generated from the projection of Lagrangian liquid spray, and the liquid penetration is defined by threshold values of $2e-6$ and $2e-7$. It is possible to see that the liquid length computed from a higher threshold value agrees better with the measured data. This might be attributed to the neglect of the atomization process, which leads to slower evaporation and faster liquid penetration due to the larger droplet size. The inclusion of atomization sub-model might improve the prediction, which is of great interest for future investigation. The computed vapor penetration evidences a rather good agreement with experiments, which is a prerequisite for proceeding to combustion simulations and further validation of the numerical setup was reported in [35].

A 156-species, 3370-reaction mechanisms proposed by Frassoldati et al. [52–54] was used to model the oxidation of PRFs, whose validity was comprehensively assessed in [52], considering the predictions of ignition delay times for stoichiometric fuel/air mixture of a gasoline surrogate (ternary mixture of iso-octane, n-heptane and toluene) at 15 and 50 bar, as well as the laminar flame speeds for neat iso-octane, n-heptane, toluene and a ternary mixture at 298 and 358 K. Specific tables were generated for each fuel blend. Table 2 reports the details of table discretization: 33 points were used to discretize the mixture fraction space and seven stoichiometric scalar dissipation rates were chosen, following a logarithmic curve. Such discretization represents a good compromise between accuracy and computational costs, and any further increase in table resolution does not significantly improve the results. The ignition delay and lift-off length are chosen as two combustion indicators for the validation of the TFPV approach, which are defined according to the suggestions from ECN: ignition delay is computed as the time from the start of injection to the time where the rising rate of maximum temperature reaches the highest value; lift-off length is identified as the axial distance from the injector orifice to the first location where the OH mass fraction reaches 14% of its maximum value in CFD domain. The computed and measured ignition delay and lift-off length are compared in Fig. 6, which indicates that the numerical models correctly predict the trend of the ignition delay and lift-off length as a function of PRF number, including: 1. a gradual increase of ignition delay and lift-off length with the increase of PRF number from PRF0 to PRF60; 2. a significant increase in the slope when changing from PRF60 to PRF80. It demonstrates that the current computational setup could correctly predict the increase of premixed combustion portion and proves its reliability and validity of providing an in-depth analysis of combustion and soot formation characteristics for these five operating points. Not to be ignored, the ignition delay is over-predicted in simulations. However, it might be related to the description of the mixing process rather than the combustion model. In particular, neglecting the atomization process could lead to slower evaporation and fuel-air mixing, as well as a subsequent longer ignition delay. The underestimation of lift-off length can also be observed, which might be explained by the diffusion of progress variable, which could facilitate the

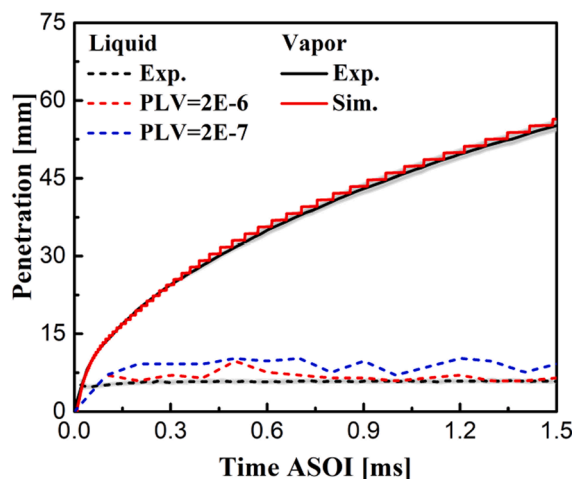


Fig. 5. Computed and measured liquid and vapor penetrations.

Table 2
Chemistry table discretization.

Temperature [K]	800, 850, 900, 950, 1000
Pressure [bar]	50, 60, 70
Equivalence ratio	0–0.7: step 0.1 0.7–1.4: step 0.05 1.4–2: step 0.1 2–3: step 0.2
mixture fraction segregation	0, 0.001, 0.005, 0.01, 0.05, 0.1, 1
Scalar dissipation rate χ_{st} [s^{-1}]	0, 1, 3, 7, 20, 55, 100

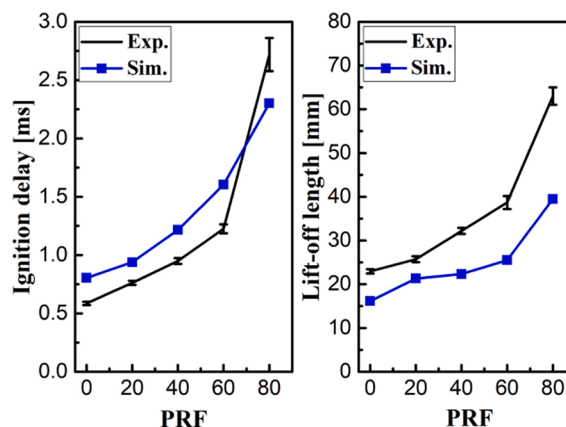


Fig. 6. Comparison between measured and computed ignition delay and lift-off length as a function of PRF number at baseline condition.

combustion in the upstream of the spray jet and make the flame stabilize more upstream. More efforts will be dedicated to overcome this issue.

3.1. Combustion characteristics

In the following discussion, the analysis technique of integrated plots is thoroughly used to study temporal and spatial features of the flame structure and soot characteristics. Such technique has been widely used in both experimental and numerical Diesel spray studies [55] [56] [35], known as intensity-axial distance-time (IXT) plot. CFD information being relevant to the combustion and emission features, such as hydroxyl (OH), formaldehyde (CH_2O), and acetylene (C_2H_2) mass fractions, soot volume fraction are integrated along the symmetry axis in present work, according to:

Table 1
Computational setup.

	Models
Turbulence	Standard $k-\epsilon$ ($C_1 = 1.50$)
Spray evolution	Eulerian-Lagrangian
Injection distribution	Rosin-Rammler
Spray breakup	Reitz-Diwakar
Droplet evaporation	D^2 law & Spalding mass number
Droplet heat transfer	Ranz-Marshall
Collision	None

$$I(x, t) = \int_0^R I(x, r, t) dr \quad (23)$$

where I is the intensity (mass fraction), x is the axial direction, r is the radial direction, and R is the radial limit. Following this approach, the OH and CH_2O mass fractions, the indicators for low- and high-temperature combustion, are integrated, normalized and plotted against the time after the start of injection and axial distance in the upper panel of Fig. 7, directly compared with the apparent heat release rate (AHRR) displayed in the lower part. The filled and dashed contours represent the OH and CH_2O IXT plots, respectively, and their outer borders are illustrated by white solid and dashed lines accordingly. Various combustion features, such as ignition, flame lift-off, combustion recession, flame tip, and burn out, are exhibited in Fig. 7 (a), which clearly describes the entire combustion event for PRF0:

1. The first-stage ignition starts with the initial appearance of CH_2O , which is further formed during the progression of the cool-flame event. Then, high-temperature ignition results in a consumption of previously produced CH_2O and a formation of OH , followed by an intense peak in AHRR;
2. Mixing controlled combustion takes place, where the flame is stabilized at the lift-off location and AHRR reaches an almost stable value;
3. The near-nozzle mixtures instantly undergoes a low-temperature oxidation after the end-of-injection (EOI), accompanied by the high-temperature combustion recession, where the lifted flame propagates back towards the injector nozzle, leading to the presence of two small bumps in the AHRR curve.

All these characterizations can also apply to the PRF20 case (Fig. 7 (b)), demonstrating that a slight increase in fuel RON does not significantly change the structures of a turbulent Diesel spray flame. For the remaining higher RON cases (Fig. 7(c-e)), the combustion recession, which is relevant to fuel, ambient conditions, and the EOI transient [57], is less evident or even absent. Particularly in the case of PRF80 (Fig. 7 (e)), the flame stabilizes relatively further downstream, and the entrainment wave generated after the EOI rapidly over leans the near-nozzle mixtures, making it incapable of second-stage ignition, which leaves a large region of partially oxidized mixture upstream. This could contribute to the unburned hydrocarbon (UHC) and CO emissions, indicated by a lower combustion efficiency in Table 3, which reports the energy allocation for different fuels at 5 ms. The combustion efficiency is defined as the ratio between the cumulative heat release and the total input energy (*injected mass * fuel lower heating value*). Such observation confirms the findings in [16] that more UHC emissions were produced in the GCI engine using PRF90 and suggests to support the combustion recession in the GCI engine, which needs a proper modulation of injection to control the EOI entrainment transient in the jet. Note that the conventional Diesel injection strategies are not appropriate to be directly applied to the GCI engine, as they are generally designed to suppress the combustion recession to reduce soot emission, which will be discussed in Fig. 11.

Regarding the change of ignition behavior during the transition from Diesel-like (PRF0) to gasoline-like (PRF80) fuels, we can mention the increased high-temperature ignition delay and the more vigorous AHRR peak owing to the higher amount of premixed charge as reported in Table 3. It highlights that the premixed portion of cumulative heat release rate increases by a factor of 3.5 when changing from PRF0 to PRF80, particularly 21.39% of fuel is burned in premixed conditions in the PRF80 case. For what concerns the steady-state burning phase, it is possible to see that the lift-off length, determined by the co-dependency of mixing and chemistry, increases non-linearly with the iso-octane content, as also observed in experiments (Fig. 6). Such change could enhance the quantity of air entrained into the spray prior to the lifted flame, and in turn, increase the oxygen entered in the central rich

reaction zone that appears just downstream of the flame stabilized location [58]. It explains why the faster depletion of CH_2O and the more intensified high-temperature combustion occur during the steady-state burning phase when shifting from PRF0 to PRF80 (in Fig. 7).

Fig. 8 compares the distributions of progress variable source term, namely the reaction rate, for PRF0, PRF40, and PRF80 in the steady-state burning phase (3.3 ms). The high-temperature reaction zones, defined by the threshold value of 2% maximum OH mass fraction, are indicated by solid red lines, and the white ones depict the premixed regions, which is identified by the flame index (FI) [59,60]:

$$FI = \frac{\nabla Y_{Fu} \cdot \nabla Y_{Ox}}{|\nabla Y_{Fu} \cdot \nabla Y_{Ox}|} \quad (24)$$

here, the subscripts Fu and Ox refer to the fuel and oxidizer components, calculated follow [61]: $Y_{Fu} = Y_{C_8H_{18}} + Y_{NC_7H_{16}} + Y_{CO} + Y_{H_2}$ and $Y_{Ox} = Y_{O_2} + Y_O$. The flame index is negative when combustion is in the diffusion-flame mode, while it is positive in the premixed region. PRF0, PRF40, and PRF80 have similar flame structure: rich premixed zone near the injector with a very intense reaction just downstream. Then, the flame develops and stabilizes in a diffusion manner, having small pockets of lean premixed high-temperature reaction in the spray periphery. In the PRF80 case, a larger premixed high-temperature combustion appears right after the very intense reaction. This is probably due to the high air entrainment and low scalar dissipation rate around the lift-off location, which promotes the high-temperature oxidation of local premixed charge to take place.

3.2. Sooting characteristics

Reducing the soot emission is the primary goal of increasing the fuel RON in CI engines, which needs an in-depth understanding of how the changes in chemistry and mixing introduced by such a shift of fuel contents affect the soot formation and distribution. A study on that will be presented in this section using the Leung-Lindstedt and Jones (LLJ) model, whose constants were tuned and validated in [35]. Fig. 9 compares the computed soot mass for different PRFs, and the data are normalized with respect to the maximum value of the PRF0 case. It is possible to see that the quasi-steady value of soot mass does not monotonically decrease with the fuel RON, and two main observations can be made: 1. the amount of soot is significantly reduced from PRF40 to PRF80; 2. the highest soot mass is presented in PRF20, and from PRF0 to PRF40, the soot trend is PRF0 < PRF40 < PRF20.

Regarding the first point, a possible explanation could be found in Fig. 10, where the soot mass is normalized with respect to the maximum value of each fuel and colored in the equivalence ratio-temperature plot at three instants, representing the initial, growth and steady states. The black lines depict the bound of equivalence ratio and temperature in the computational domain. Comparing the soot evolution for PRF40 (Fig. 10 (b)) and PRF80 (Fig. 10(c)), it is quite clear that the soot mitigation is achieved by enhanced mixing, owing to the higher lifted flame. In particular, the maximum equivalence ratio in PRF80 is about 1.6, which is not an ideal condition for soot formation. Such an impact is less pronounced when shifting from PRF0 to PRF40, since the presence of a sufficiently rich mixture could still favor the production of soot. Besides, an increase in temperature from PRF0 (Fig. 10 (a)) to PRF40 (Fig. 10(b)) could even promote nucleation of soot precursors and surface growth of soot particles. This might be a possible elucidation for the second observation in Fig. 9. To deepen the exploration and understanding of this point, the integrated soot volume fraction (SVF) and C_2H_2 mass fraction, the soot-precursor, are overlaid in Fig. 11, displayed by filled contours and hatched patterns, respectively. For better visualization, data are normalized according to the maximum values encountered in each chart. The maximum values of SVF are then plotted in Fig. 12 to give a quantitative assessment and comparison of soot formation characteristics for different fuels. The bounds of $I_{normalized,OH} = 0.02$ and

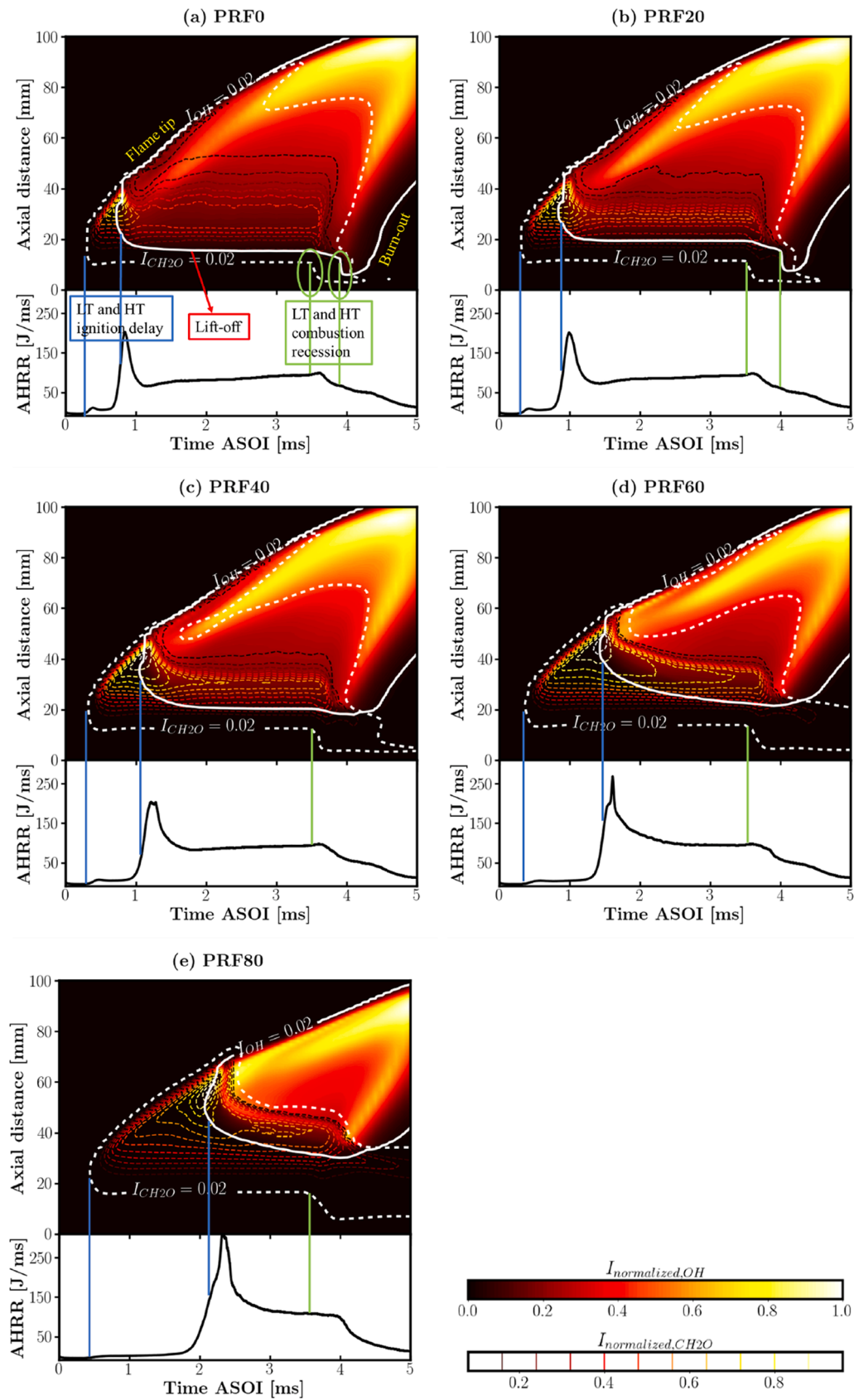


Fig. 7. AHRR and IXT plots of CH_2O (dashed contour lines) and OH for different fuels: (a) PRF0, (b) PRF20, (c) PRF40, (d) PRF60, (e) PRF80. Data are normalized according to the min–max values encountered in each chart. White solid and dashed lines represent $I_{normalized,OH} = 0.02$ and $I_{normalized,CH_2O} = 0.02$, respectively. Various features are indicated in (a): low and high temperature ignition are identified by blue lines; low and high combustion recession are shown in green circles.

Table 3

Energy allocation for different fuels at 5 ms.

Fuel	Total energy	Cumulative HRR	Combustion efficiency	Premixed HRR	Premixed portion
PRF0	368.2 J	355.6 J	96.58%	22.2 J	6.24%
PRF20	367.8 J	355.5 J	96.66%	26.1 J	7.24%
PRF40	367.3 J	354.9 J	96.62%	32.3 J	9.10%
PRF60	366.9 J	353.8 J	96.43%	44.8 J	12.66%
PRF80	366.4 J	347.3 J	94.79%	74.3 J	21.39%

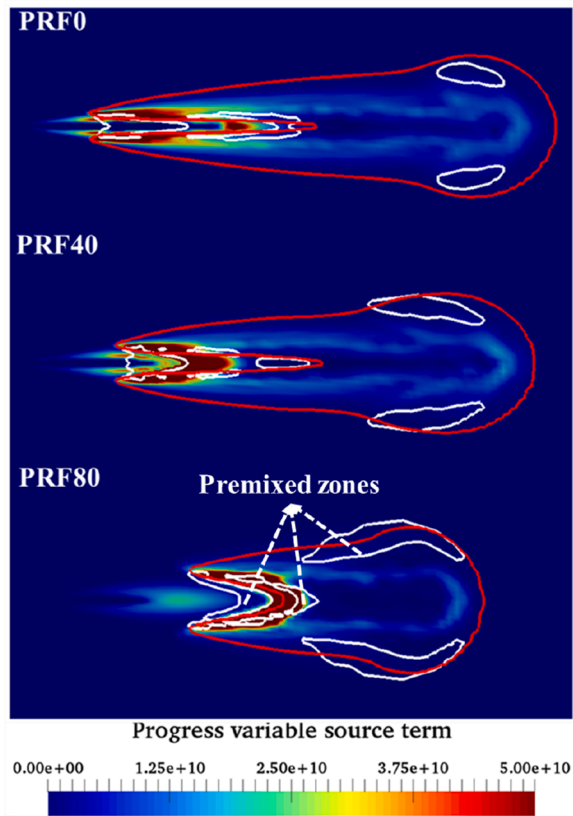


Fig. 8. Progress variable source term distributions for PRF0, PRF40, and PRF80 at $t = 3.3$ ms. The premixed zones ($FI > 0$) are identified by white solid lines, while the high-temperature zones, where the OH mass fraction reaches 2% of its maximum value red solid lines are indicated by red solid lines.

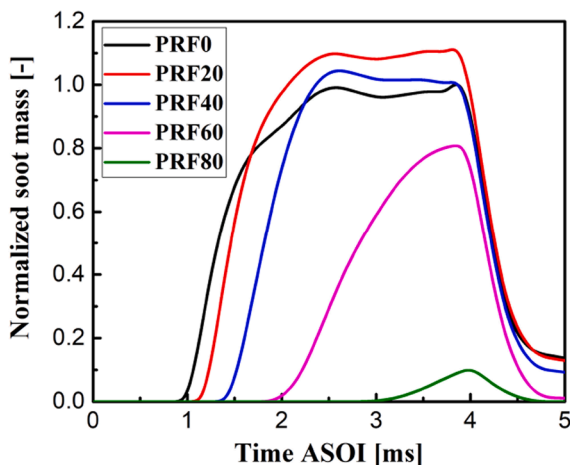


Fig. 9. Computed soot mass for different PRFs. Values are normalized with respect to the maximum value of PRF0.

$I_{normalized,CH_2O} = 0.02$ are also presented using solid black and red lines, respectively, to describe the connection between combustion and soot formation features. From PRF0 to PRF40, the highest SVF intensity appears shortly after the ignition event and slightly downstream of the ignition location, where the CH_2O formed during the entire cool-flame phase abruptly depletes and produces a high amount of C_2H_2 and soot due to the lack of oxidation. However, this does not apply to PRF60 and PRF80, where enhanced fuel–air mixing at the onset of combustion does not favor the formation of soot, and the SVF intensity in the central region of spray increases gradually over time as a consequence of the reduction of lift-off length. In Fig. 11 (a), soot recession and first-soot distance, defined as the distance from the injector to the first sooting region, are marked. Comparisons and observations can be made for different fuels considering these two aspects:

- **First-soot distance:** In Fig. 11, it is possible to see that PRF80 has the highest first-soot location, while the longest distance between lift-off and first soot-forming region occurs in PRF0. This distance, together with the jet velocity, is the evidence to estimate the approximate soot inception time, which depends on fuel sooting-propensity and operating conditions [62]. Table 4 summarizes the lift-off length, first-soot distance, and soot inception time calculated based on the spray velocity along the centerline. The soot inception time increases with the fuel RON when moving from PRF40 to PRF80. However, from PRF0 to PRF40, the trend appears as $PRF0 > PRF40 > PRF20$. It is noteworthy that such trend can well represent the change of soot mass with fuel content shown in Fig. 9: a short soot inception time indicates a high sooting propensity, and consequently, an increased amount of soot. From the modeling perspective, owing to the simplicity of the soot model, the soot inception time depends on the C_2H_2 concentration and the local temperature at the lift-off location, where a vigorous high-temperature reaction occurs. Shifting from PRF0 to PRF20, a higher amount of CH_2O is formed prior to the flame stabilized location as a consequence of elongated cool-flame duration, indicated by the longer distance between the lower edge of $I_{normalized,OH} = 0.02$ and $I_{normalized,CH_2O} = 0.02$, which could facilitate the production of heat and the formation of C_2H_2 at the lift-off location, and in turn, reduce the soot inception time.
- **Soot recession:** from PRF0 to PRF40, the mixture upstream of the lifted flame remains still fuel-rich after the EOI entrainment wave and is sufficient to promote the second-stage combustion and soot formation, resulting in a recession event and a bump in soot mass (Fig. 9) prior to the ramp-down phase. This could be overcome by enhancing the air entrainment upstream of the lift-off location, which could be achieved either by inducing a strong EOI transient as mentioned in Fig. 7 or moving the lifted flame further downstream. The second potential consideration has been proven in Fig. 11 (d) and (e), where soot recession does not take place due to the high lift-off location and the consequent enhancement of mixing.

4. Heavy-Duty CI engine

The Sandia optical engine, a single-cylinder, direct-injection (DI), 4-stroke Diesel engine based on a Cummins N-series production, was used in this investigation. Details of the piston bowl geometry are shown in Fig. 13, and the specifications of the engine are summarized in Table 5. A more complete description of the engine is available in [63,41]. The spray-oriented mesh was automatically generated using the algorithms presented in [49] to represent a 1/8 sector of the combustion chamber as illustrated in Fig. 13. The mesh has 49010 cells at IVC which are reduced to 12194 at TDC owing to the use of dynamic layering technique during mesh motion [49]. Simulations start at IVC with a flow field imposed by assuming a wheel-flow velocity profile whose intensity is proportional to the swirl number measured at the flow bench under steady-state flow conditions. Three different operating conditions were selected from [41]

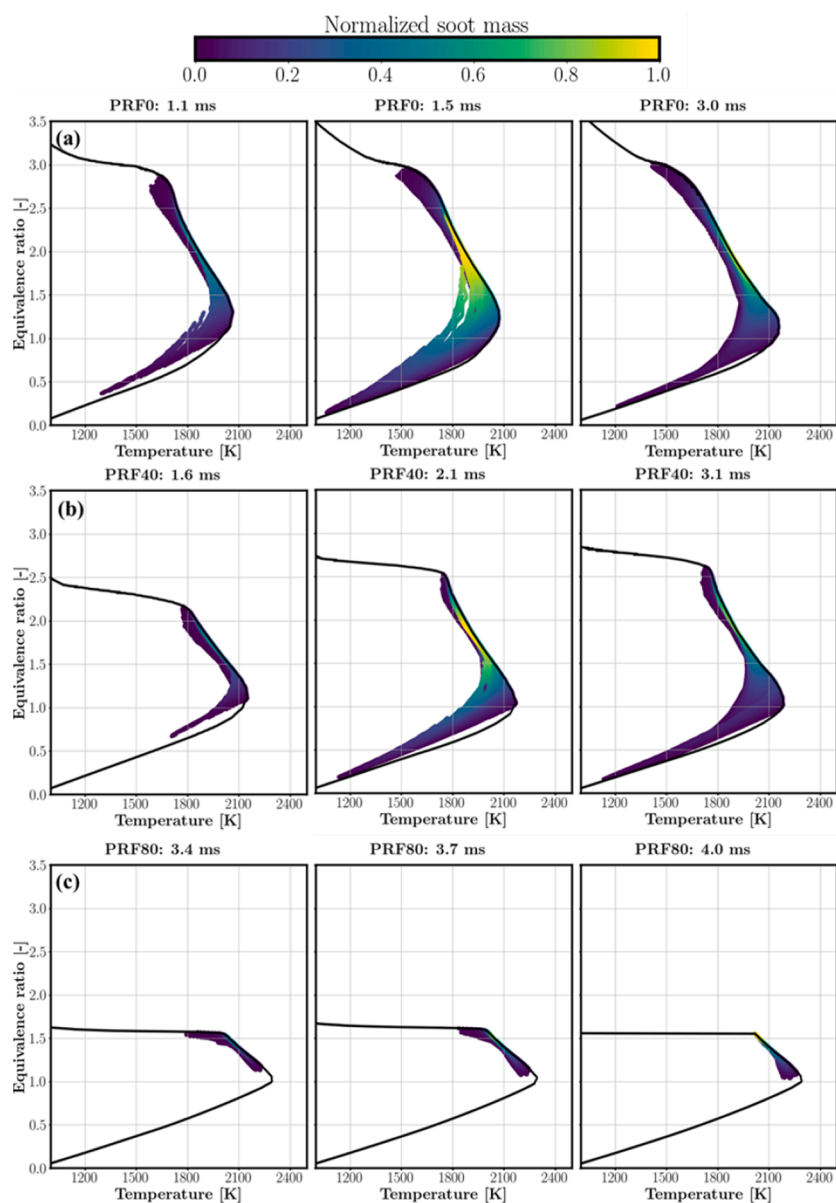


Fig. 10. Equivalence ratio-temperature plot with normalized soot mass colored at for at three instants, representing the initial, growth, and steady evolution states for (a) PRF0; (b) PRF40; (c) PRF80. Normalization is performed with respect to the maximum value for each PRF.

to first validate the TFPV model in practical engine combustion modeling. Details of these operating conditions are reported in Table 6. The first condition, HTSID (High-T, Short-ID), is typical of conventional diesel combustion, with a short ignition delay, while the two remaining points, LTEInj and LTLInj, are characterized as LTC operating conditions with early and late injection timings, respectively. *n*-heptane was used to represent the auto-ignition behavior of diesel. The injected mass was corrected according to their difference in lower heating value (LHV) to keep the total input energy identical with experiments, but preserving the same injection duration and adjusting the area contraction coefficient to maintain the same spray momentum. Two chemistry tables were generated according to the chemical compositions at IVC. Details of the table discretization are presented in Table 7, similar as the one for combustion vessel simulations (Table 2). Large temperature and pressure ranges were considered to take into account all the expected thermodynamic states encountered in IC engine simulations. Such choice of chemistry table discretization has been comprehensively validated and assessed in [37,36,29], which is a good compromise between accuracy and table size, and further refinement of the table resolution does not

show any improvement in the results. Note that the unsteady diffusion flamelet calculations were performed only within a 750–1200 K temperature range to reduce the computational cost, and tables were later extended to 400 K with values from homogeneous reactor chemistry tables.

Fig. 14(a)–(c) report the comparison between the computed and measured in-cylinder pressure and AHRR for all these three conditions, showing rather good agreement between simulations and experiments. A slight overestimation of ignition delay could be attributed to two aspects: first, the spray sub-models that neglect of atomization process could lead to longer ignition delays as discussed in Fig. 6; second, the chemistry that *n*-heptane is used as the representative of the actual Diesel fuel, which is less reactive and has longer ignition delay. These also explain why the models over-predict the onset of soot formation and the appearance of the peak value in Fig. 15, which compares the measured and computed normalized in-cylinder soot evolution for the HTSID condition. Except for such discrepancy, it is possible to see that the critical soot formation and oxidation trends are very well described by the chosen models. Soot prediction was not considered in the other

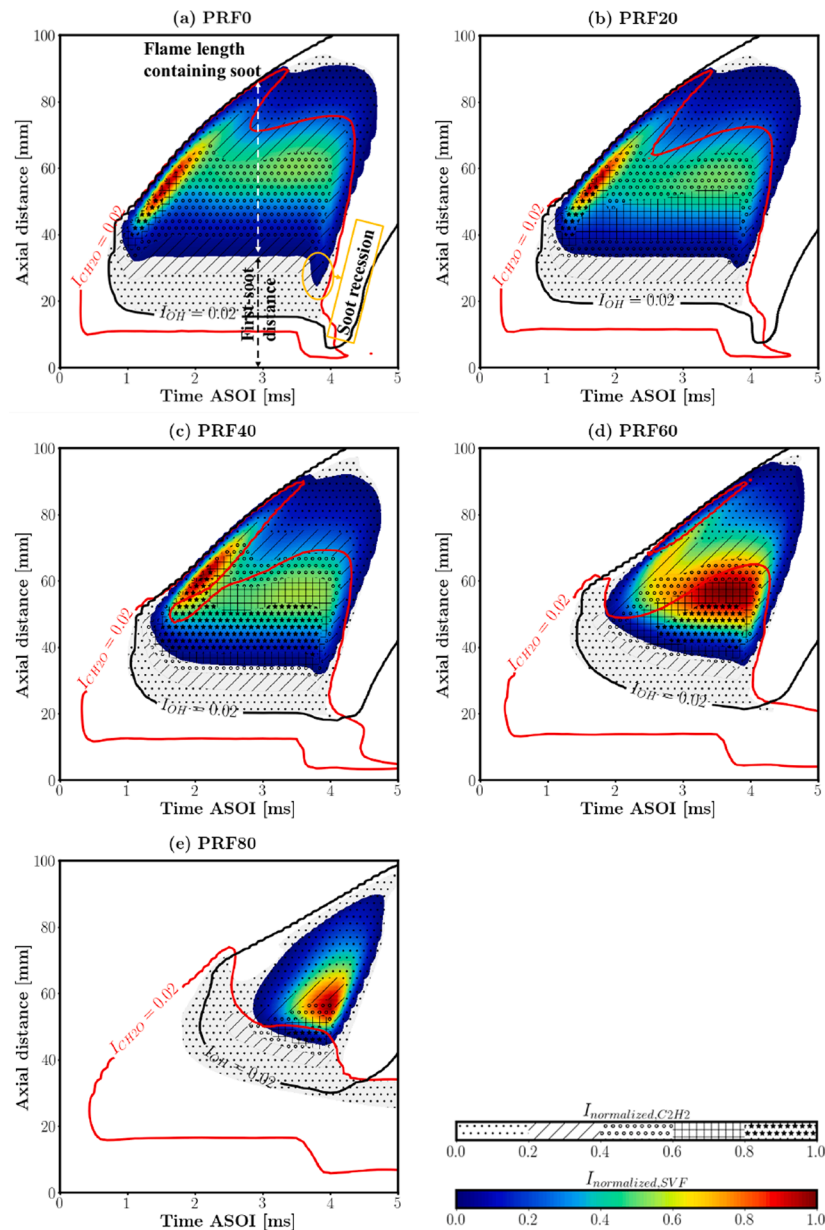


Fig. 11. IXT plots of soot volume fraction (filled contours) and C_2H_2 (hatched patterns) for different fuels: (a) PRF0, (b) PRF20, (c) PRF40, (d) PRF60, (e) PRF80. Data are normalized according to the min–max values encountered in each chart. Black and red solid lines represent $I_{normalized, OH} = 0.02$ and $I_{normalized, CH_2O} = 0.02$, respectively.

two LTC operating conditions due to its less evident presence. In Fig. 16, the NO_x evolution is illustrated and compared with the measured engine-out values for the HTSID and LTEInj conditions, indicating that the tabulated NO_x model could accurately predict the NO_x values for both conventional and LTC engines. A slight underestimation of NO_x values might be explained by the lack of turbulence-chemistry interaction in the tabulated NO_x model that could postpone the formation of NO_x in the cylinder with a consequence of slightly lower engine-out NO_x emission. Besides, its in-cylinder evolution is also correctly described: NO_x accumulates during the combustion process and stabilizes at its maximum value when in-cylinder thermodynamic conditions are not able to promote any additional NO_x formation. Further validation of this NO_x model can be found in [29,37]. Following such satisfactory accuracy of pressure, AHRR, soot, and NO_x predictions, a numerical co-optimization of fuel auto-ignition quality and injection timing was performed for the conventional Diesel operating condition (HTSID) considering ten PRFs from PRF0 to PRF90 with 10% increment in iso-

octane mass fraction. Fuels were delivered at different SOIs, from -5 to -13° ATDC, to find an optimum injection timing and make the best use of various fuels. The original HTSID operating condition using PRF0 (n-heptane) and $SOI = -7^\circ$ ATDC is defined as the baseline case. Results in terms of engine performances, soot and NO_x emissions will be discussed in this section.

4.1. Engine performance

Fig. 17 compares the computed in-cylinder pressure and heat release rate for different fuels. It is possible to see that reducing the auto-ignition propensity by moving from Diesel-like to gasoline-like fuels could postpone the high-temperature ignition event and enhance the burning rate due to the formation of large amounts of premixed charge and low-temperature oxidation products before the onset of combustion. Such aspects could potentially arise two problems:

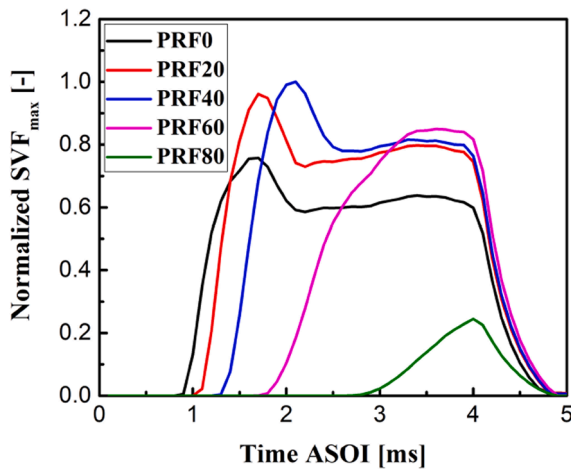


Fig. 12. Computed maximum soot volume fraction for different PRFs. Values are normalized with respect to the maximum value of all PRFs.

Table 4
Lift-off length, first soot distance and soot inception time for different fuels.

Fuel	Lift-off length	First-soot distance	Soot inception time
PRF0	15.89 mm	33.96 mm	164 μ s
PRF20	19.42 mm	33.27 mm	149 μ s
PRF40	20.28 mm	34.23 mm	159 μ s
PRF60	23.96 mm	38.00 mm	193 μ s
PRF80	34.20 mm	49.16 mm	286 μ s

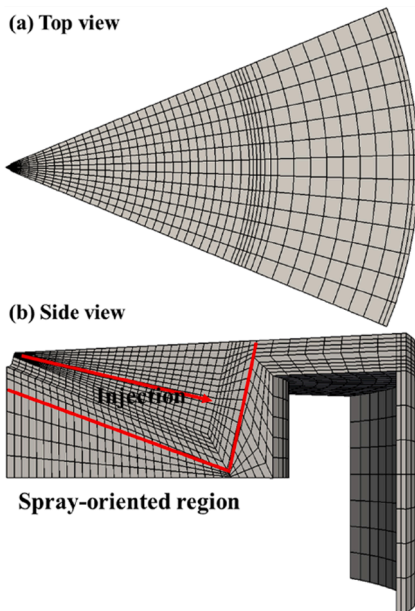


Fig. 13. Computational mesh of the Sandia optical engine.

1. High UHC and CO emission due to the retarded combustion phase and overly lean mixtures, as discussed in Fig. 7, which could be characterized by the combustion efficiency. Fig. 18 summarizes the combustion efficiencies of different fuels and injection timings, which depicts that at the tested condition, the fuel reactivity plays a more dominant role in determining the combustion efficiency compared to the injection timing. This might be explained by that compared to varying the fuel RON number, ignition delay is less affected by changing the SOI from -5 to -13 $^{\circ}$ ATDC, since the in-

Table 5
Engine specifications for simulations.

Description	Specification
Stroke	152.4 mm
Bore	139.7 mm
Connecting rod	304.8 mm
Compression ratio	16:1
Nozzle diameter	0.196 mm
Number of holes	8
Injection angle	152 deg
Exhaust Valve Open (EVO)	124 deg
Inlet Valve Close (IVC)	-165 deg
Swirl ratio	0.5

Table 6
Engine operating conditions.

	High-T, Short-ID (HTSID)	Low-T, Early-Inj. (LTEInj)	Low-T, Late-Inj. (LTLInj)
Speed	1200 rpm	1200 rpm	1200 rpm
IMEP	4.4 bar	3.9 bar	4.1 bar
P_{inj}	233 kPa	214 kPa	202 kPa
$Mass_{inj}$	61 mg	56 mg	56 mg
Fuel	Diesel	Diesel	Diesel
SOI	-7 $^{\circ}$ ATDC	-22 $^{\circ}$ ATDC	0 $^{\circ}$ ATDC
DOI	10 CAD	7 CAD	7 CAD
O ₂	21%	12.7%	12.7%

Table 7
Chemistry table discretization for engine simulations.

Temperature [K]	400–1200: step 50
Pressure [bar]	10, 30, 50, 60, 70, 80, 90
Equivalence ratio	0–0.7: step 0.1 0.7–1.4: step 0.05 1.4–2: step 0.1 2–3: step 0.2
mixture fraction segregation	0, 0.001, 0.005, 0.01, 0.05, 0.1, 1
Scalar dissipation rate χ_{st} [s^{-1}]	0, 1, 3, 7, 20, 55, 100

cylinder thermodynamic conditions do not differ too much. In particular, when changing from PRF80 to PRF90, a large premixed combustion portion resulted from a long ignition delay, together with a delayed combustion phase, could lead to a significant deterioration of combustion efficiency, indicating high UHC and CO emissions, which confirms the experimental observation in [16]. An earlier injection timing could slightly improve the combustion efficiency, which however is limited by the ringing intensity.

2. High ringing intensity (RI) due to the rapid combustion and the consequent high pressure rise rate. The RI is correlated with the acoustic energy of the resonating pressure wave to quantify the propensity of the combustion to produce acoustic oscillations [64], which is defined as [65]:

$$RI \left(MW / m^2 \right) = \frac{1}{2\gamma} \frac{[\beta(dp/dt)_{max}]^2}{P_{max}} (\gamma RT_{max})^{1/2} \quad (25)$$

where β is set to 0.05 ms and γ is the specific heat ratio; P_{max} and $(dp/dt)_{max}$ represent the maximum in-cylinder pressure and its rise rate, respectively; R is the gas constant and $(\gamma RT_{max})^{1/2}$ is the speed of sound at the maximum average in-cylinder temperature. The $RI = 5$ MW/m^2 is used as the criterion to detect the knock occurrence and avoid the knocking operating regimes [64]. The computed RIs for different PRFs and injection timings are summarized in Fig. 19, illustrating the high knocking propensity when using PRF80 and PRF90 due to the very intensive premixed combustion and AHRR. A retarded injection timing could reduce the RI, but meantime

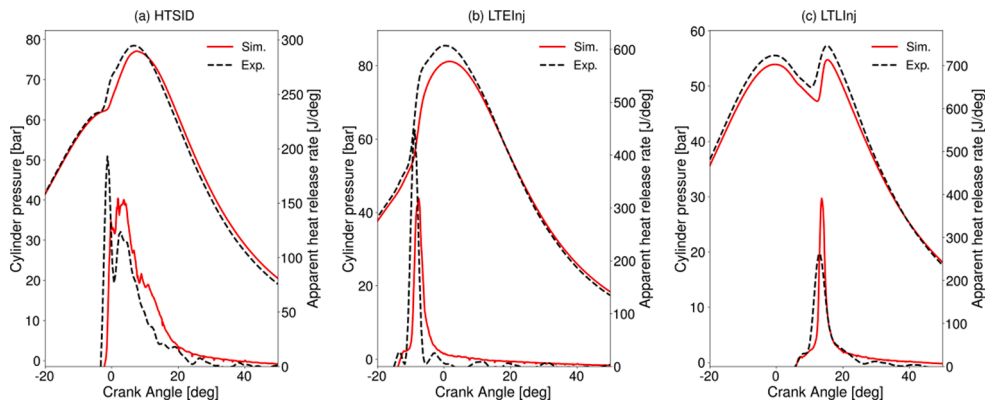


Fig. 14. Comparison between experimental and computed in-cylinder pressure and apparent heat release rate profiles for different operating conditions: (a) HTSID; (b) LTEInj; (c) LTLInj.

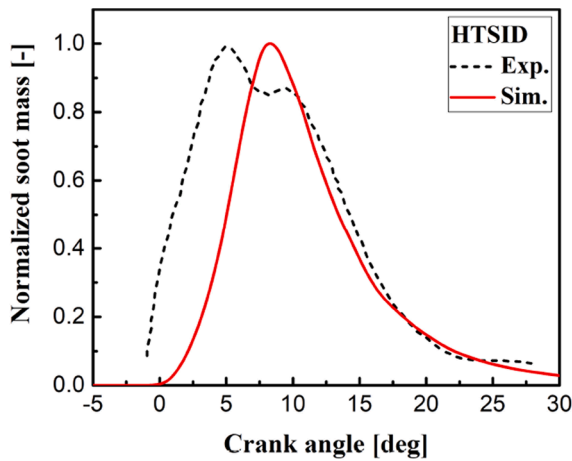


Fig. 15. Comparison between measured and computed normalized soot evolution for the HTSID operating condition.

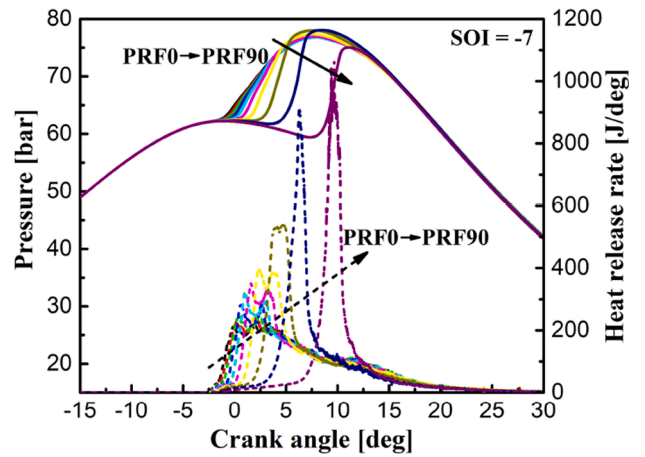


Fig. 17. Computed in-cylinder pressure and heat release rate for different PRFs with SOI = -7 ° ATDC.

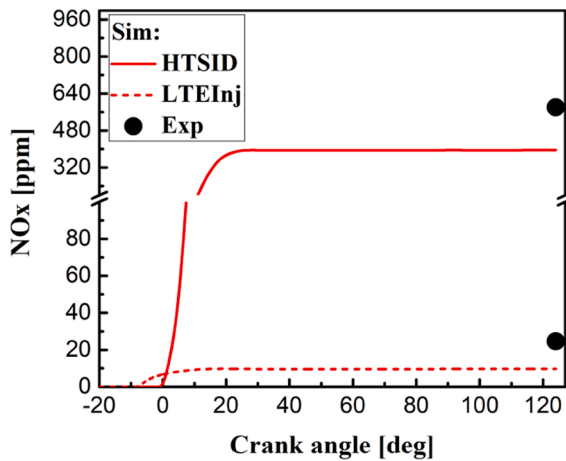


Fig. 16. Comparison between experimental and computed NO_x emissions for HTSID and LTEInj operating conditions.

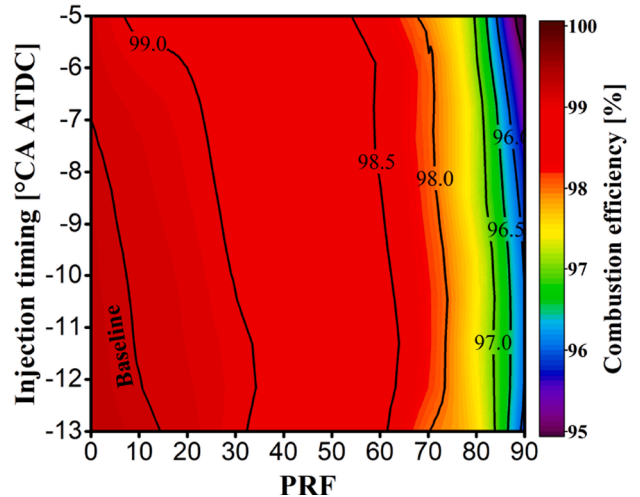


Fig. 18. Computed contours of the combustion efficiency for different fuels and injection timings.

deteriorate the combustion efficiency (Fig. 18), indicating the presence of the “trade-off” relation between knocking probability and combustion efficiency in premixed dominated combustion mode.

The gross indicated efficiency (GIE) that reflects the total work yielded by the combustion of the fuel is reported in Fig. 20 for different

fuels and injection timings. Two operating regimes that show comparable or even superior performance to the baseline case are of interest:

1. PRF0–PRF30 with SOI varying from -7 to -12 ° ATDC: This suggests that in a conventional CI engine, a reduced fuel auto-ignition quality

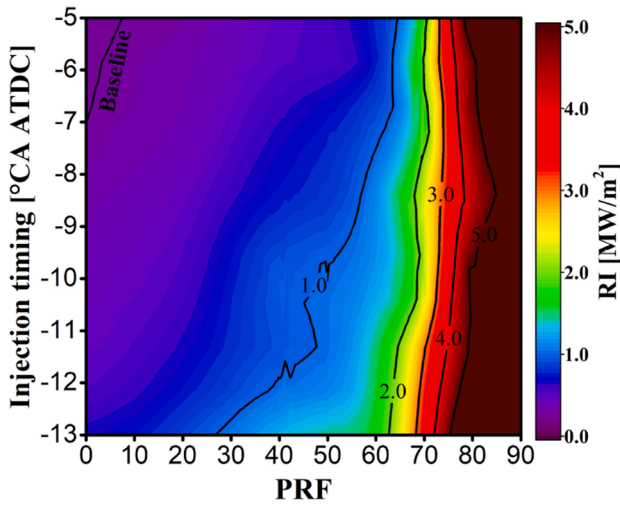


Fig. 19. Computed contours of the ringing intensity for different fuels and injection timings.

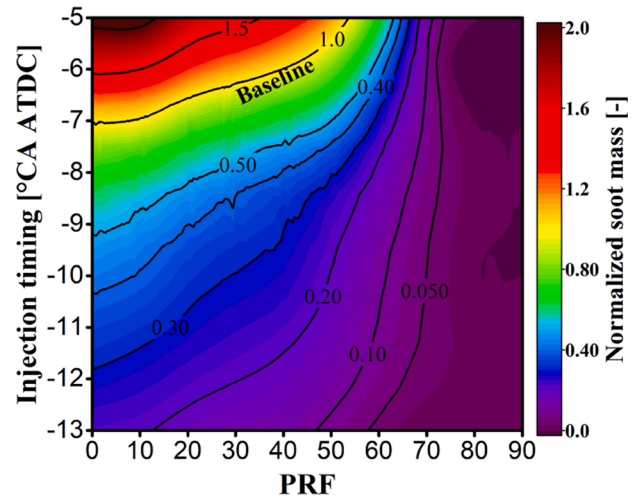


Fig. 21. Computed contours of the soot mass for different fuels and injection timings. Data are normalized with respect to the baseline value.

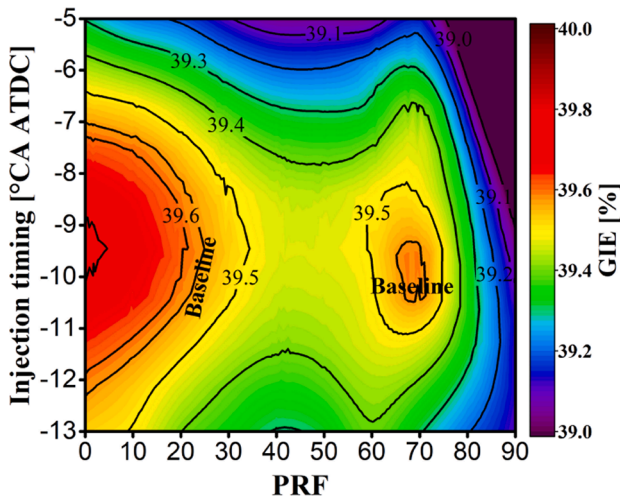


Fig. 20. Computed contours of the gross indicated efficiency for different fuels and injection timings.

realize a considerable soot mitigation by allowing a better mixture preparation before the ignition event. However, this could lead to an increase in NO_x emission, as illustrated in Fig. 22, which presents the computed NO_x emissions for different PRFs and injection timings. It shows that NO_x is more sensitive to the injection timing, and possible reasons can be found in Fig. 23 and 24, which present the in-cylinder evolution of NO_x and its formation rate for different PRFs and SOIs, respectively. It can be found that for all the tested points, the engine-out NO_x emission depends on two aspects: first, the formation rate that determined by the in-cylinder thermodynamic conditions; second, the formation duration, which is from the end of high-temperature ignition to around 30° ATDC when the in-cylinder temperature cannot promote any further formation of NO_x. Looking at Fig. 23, it is possible to see that the use of high RON fuel could have two counterbalance effects on the NO_x emission: the more intensified formation rate as a consequence of vigorous heat release rate generated from premixed burn and the shorter formation duration due to the longer ignition delay and faster combustion event. In Fig. 24, advancing the injection timing could prolong the NO_x formation duration and increase its formation rate together with the piston movement, which explains the strong sensitivity of NO_x to SOI. However, the fuel RON plays a more prominent role in controlling soot emissions, and such observation reveals that the trade-off between NO_x and soot, which is a critical issue for conventional CI

by means of blending a small amount of gasoline-like fuel, together with an earlier injection timing to maintain the optimum combustion phase, could preserve the intrinsic high GIE and have the possibility to reduce the soot emissions, which will be discussed in Fig. 21.

2. PRF60–PRF70 with SOI varying from –8 to –11 ° ATDC: This represents a typical GCI engine operating regime, evidencing the potential of such a novel combustion concept to achieve a similar fuel economy and power density as standard CI engines. There are also substantial benefits of emission mitigation without any optimization of engine configuration or control system, as discussed in the next section.

Summarizing the obtained results for GIE, RI, and combustion efficiency (UHC and CO), we may conclude that suitable fuels for today’s CI engines might be a Diesel-like fuel with a RON of 0–30 or a gasoline-like fuel with a RON of 60–70.

4.2. Soot and NO_x emissions

Fig. 21 reports the computed soot mass at EVO for different operating points. Data are normalized with respect to the baseline value. It is possible to see that using an earlier injection or a less reactive fuel could

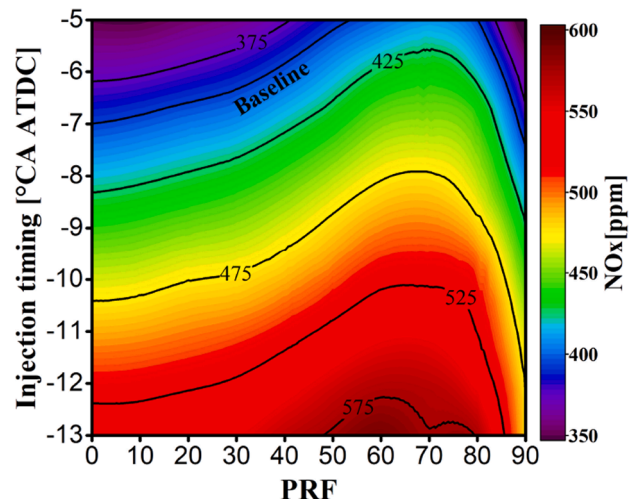


Fig. 22. Computed contours of the NO_x emission for different fuels and injection timings.

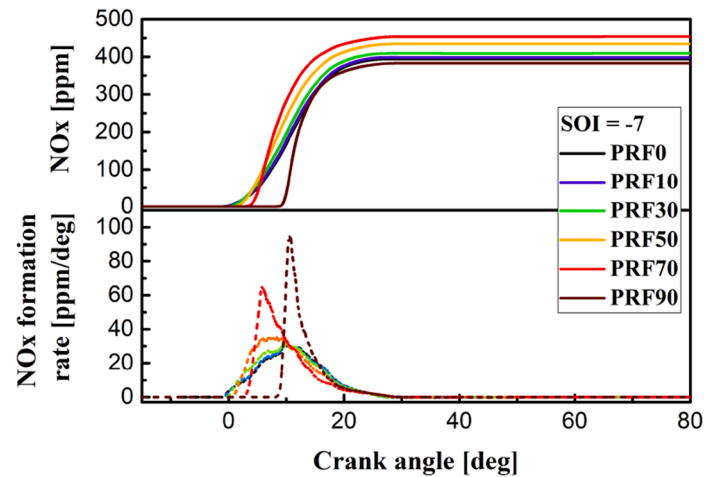


Fig. 23. Computed NO_x and its formation rate for different PRFs with SOI = -7 ° ATDC.

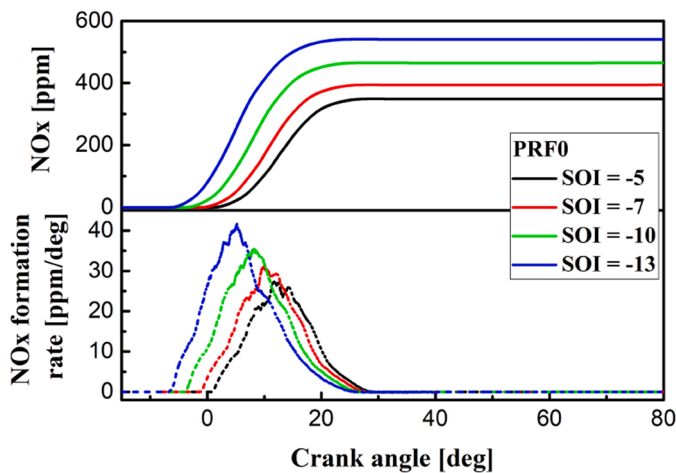


Fig. 24. Computed NO_x and its formation rate for PRF0 with different SOIs.

engines, could be defeated by shifting from Diesel-like to gasoline-like fuels. In particular, within the fuel-efficient regimes identified in Fig. 20, along the contour line of NO_x = 475 ppm (Fig. 22), the soot mass can be reduced to 40%, 35%, and 5% of the baseline value using PRF0, PRF30, and PRF70 (Fig. 21), respectively. Such results suggest that at the current operating condition, the GCI engine running with 70 RON fuel exhibits a better performance in terms of both fuel efficiency and emissions.

To deepen the understanding of how fuel RON affects the engine-out soot emission, which depends on both the formation and oxidation processes in practical engines, Fig. 25 illustrates the in-cylinder evolution of soot mass and its formation/oxidation rate for different fuels. Data are normalized with the peak values of the PRF0 case. Note that the observations and conclusions obtained from the combustion vessel simulations (Fig. 9 and Fig. 12) should be applied with care to the practical engine since most of the soot is formed after EOI at this operating condition, where no lifted flame is present. From PRF0 to PRF80, all the cases show a very similar oxidation process, while there is a significant increase in soot formation rate when moving from PRF50 to PRF80. It might be explained by the rapid burning of mixtures, leading to the acceleration of C₂H₂ formation and temperature increase, which, on the other hand, reduces the soot formation time with a consequent lower soot peak value.

In Fig. 26, the computed CA10, CA50, CA90, and soot inception and peak times are plotted as a function of PRF number with SOI = -7 ° ATDC. The other injection timings are not presented since no major

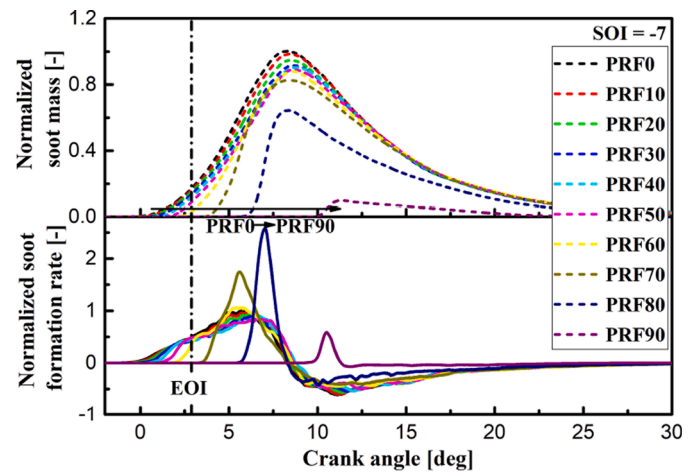


Fig. 25. Computed soot mass and its formation rate for different PRFs with SOI = -7 ° ATDC. Data are normalized with the peak values at baseline condition.

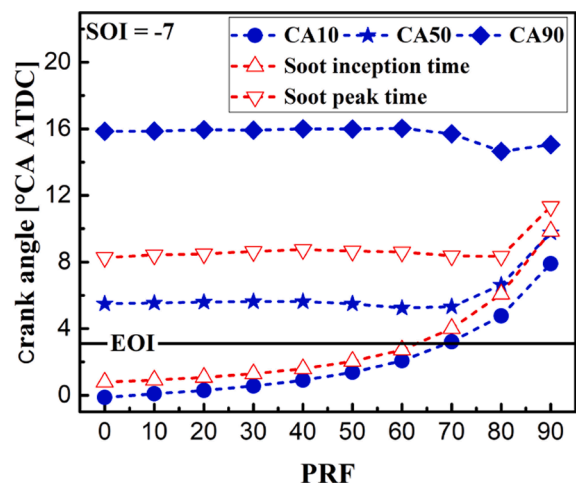


Fig. 26. Computed CA10, CA50, CA90, soot inception and peak times for different fuels with SOI = -7 ° ATDC.

difference was observed. The CA10, CA50, and CA90 represent the crank angle where 10%, 50%, and 90% of the total heat is released. The soot inception time is identified by the crank angle where 2% of the peak soot

value is reached. The crank angle difference between EOI and CA10 (start of combustion) is defined as the ignition dwell (IDW). It could be observed that the soot formation duration, from the onset of soot inception to the soot peak time, decreases with the PRF number, which is the possible explanation for soot reduction, as discussed in Fig. 25. Regarding the combustion phase, it is worth noting that the ignition (CA10) is retarded as the consequence of the poor auto-ignition propensity of high RON fuel. However, there is no obvious variation in CA50 and CA90 when altering from PRF0 to PRF70. It might be attributed to the fact that IDW remains negative or around zero during such a fuel transition, implying the establishment of the diffusion flame after the intense burning of the premixed charge, which could maintain the CA50 and CA90. To this end, an IDW around 0 might be the optimum solution since it could make the best use of conventional and advanced engines: 1. it mitigates the emissions of the conventional Diesel engine by an increased mixing time and premixed burning portion; 2. it extends the operating regime of LTC engines by controlling the burning rate and combustion phase with the subsequent diffusion flame. This might be the reason why PRF70 achieves the best performance concerning fuel efficiency and emissions at current operating condition. A wide range of engine operating conditions should be considered to confirm this finding, which will be of great interest in future work.

5. Conclusions and outlook

A comprehensive numerical study of combustion and emission characteristics of primary reference fuels (PRFs) was performed in the Diesel-like spray combustion vessel and the heavy-duty CI engine using Tabulated Flamelet Progress Variable (TFPV) approach. The temporal and spatial characteristics of the flame structure and soot formation under baseline constant-volume combustion condition were investigated and compared for different fuels from PRF0 (n-heptane) to PRF80 (20% n-heptane, 80% iso-octane), representing the transition from Diesel-like to gasoline-like fuels. Then, a co-optimization of fuel auto-ignition quality and injection timing was performed for the high-temperature, short-ignition delay (HTSID) Diesel engine operating condition considering 10 PRFs, from PRF0 to PRF90 with 10% increment in iso-octane mass fraction, and altering the SOI from -5 to -13° ATDC. Key findings and suggestions that originated from the presented results can be summarized as follows:

1. Diesel-like spray combustion vessel

- In both simulations and experiments, a non-linear increase in ignition delay and lift-off length with PRF number could be observed, with the latter one enriching air quantity in the upstream mixture of the lifted-flame. It could then accelerate the depletion of cool-flame products (CH_2O), and in combination with the low local scalar dissipation rate, promote a high-temperature premixed combustion to take place near the lift-off location.
- In low RON cases, a combustible rich mixture was formed in upstream of the lift-off location after the transient EOI entrainment wave, resulting in a high-temperature combustion recession and a consequent “flashback” of soot. Using high RON fuel could overcome this issue, which, however, may potentially increase the UHC and CO due to the absence of high-temperature oxidation of overly lean mixture upstream of the lifted flame. A proper manipulation of the EOI transient might be an ideal solution for such an issue, which will be one of the interesting future investigations.
- The soot inception time, describing the sooting propensity at the lift-off location, could well represent the trend of soot mass with the fuel content. The shortest inception time, as well as the highest soot mass, was observed in PRF20, implying a non-monotonic effect of fuel RON on soot formation under the Diesel engine conditions. Such a result emphasizes that in low RON cases, where flame stabilizes in the fuel-rich mixture near the injector, a slight increase in the lift-off length and air enrichment resulted from the addition of iso-octane could

boost the heat release, temperature, and the C_2H_2 formation at the lift-off location, thereby increasing the sooting propensity and deteriorating the soot emission.

2. Heavy-Duty CI engine

- A Diesel-like fuel with a RON of 0–30 or a gasoline-like fuel with a RON of 60–70 could preserve the intrinsic high fuel efficiency of Diesel engine. Further increase in RON (PRF80 and PRF90) could lead to the reduction of combustion efficiency due to the overly lean mixtures, which is not fully oxidized and remains as UHC and CO after the combustion event. An earlier injection timing could slightly improve the efficiency, but with the sacrifice of intensifying the ringing intensity.
- Shifting from low RON to high RON fuel could successfully defeat the trade-off between NO_x and soot in CI engines. With the same increase in NO_x and maintaining an optimum fuel efficiency, the soot mass can be reduced to 40%, 35%, and 5% of the baseline value using PRF0, PRF30, and PRF70, respectively. Concerning both fuel efficiency and emissions, the best performance is obtained by PRF70 at the current operating condition.

CRedit authorship contribution statement

Qiyang Zhou: Writing - original draft, Software, Validation, Investigation, Formal analysis. **Tommaso Lucchini:** Writing - review & editing, Conceptualization, Software, Resources, Supervision. **Gianluca D’Errico:** Conceptualization, Software, Resources, Supervision. **Ricardo Novella:** Writing - review & editing, Resources. **Jose Maria Garcia-Oliver:** Writing - review & editing, Resources. **Xingcai Lu:** Supervision, Project administration, Funding acquisition.

Declaration of Competing Interest

The authors declare that there is no conflict of interest.

Acknowledgements

Authors acknowledge the financial support from the China Scholarship Council (No. 201806230180) and Natural Science Foundation of China (No. 51961135105) for the first author’s study in Politecnico di Milano, Italy

References

- [1] Badami M, Mallamo F, Millo F, Rossi EE. Influence of multiple injection strategies on emissions, combustion noise and BSFC of a DI common rail diesel engine. *SAE Trans* 2002;111:1118–29.
- [2] Zhao F, Asmus TN, Assanis DN, Dec JE, Eng JA, Najt PM. Homogeneous Charge Compression Ignition (HCCI) Engines, SAE Technical Paper PT-94 (2003).
- [3] Selim MYE. Sensitivity of dual fuel engine combustion and knocking limits to gaseous fuel composition. *Energy Convers Manag* 2004;45(3):411–25. [https://doi.org/10.1016/S0196-8904\(03\)00150-X](https://doi.org/10.1016/S0196-8904(03)00150-X).
- [4] Reitz RD, Duraisamy G. Review of high efficiency and clean reactivity controlled compression ignition (RCCI) combustion in internal combustion engines. *Prog Energy Combust Sci* 2015;46:12–71. <https://doi.org/10.1016/j.peccs.2014.05.003>.
- [5] Qian Y, Wang X, Zhu L, Lu X. Experimental studies on combustion and emissions of RCCI (reactivity controlled compression ignition) with gasoline/n-heptane and ethanol/n-heptane as fuels. *Energy* 2015;88:584–94. <https://doi.org/10.1016/j.energy.2015.05.083>.
- [6] Qian Y, Ouyang L, Wang X, Zhu L, Lu X. Experimental studies on combustion and emissions of RCCI fueled with n-heptane/alcohols fuels. *Fuel* 2015;162:239–50. <https://doi.org/10.1016/j.fuel.2015.09.022>.
- [7] Kokjohn SL, Hanson RM, Splitter DA, Reitz RD. Experiments and modeling of dual-fuel hcci and pcci combustion using in-cylinder fuel blending. *SAE Int J Engines* 2009;2(2):24–39. <https://doi.org/10.4271/2009-01-2647>.
- [8] Jeon J, Lee JT, Kwon SI, Park S. Combustion performance, flame, and soot characteristics of gasoline-diesel pre-blended fuel in an optical compression-ignition engine. *Energy Convers Manag* 2016;116:174–83. <https://doi.org/10.1016/j.enconman.2016.03.003>.
- [9] Du J, Sun W, Guo L, Xiao S, Tan M, Li G, Fan L. Experimental study on fuel economies and emissions of direct-injection premixed combustion engine fueled

- with gasoline/diesel blends. *Energy Convers Manag* 2015;100:300–9. <https://doi.org/10.1016/j.enconman.2015.04.076>.
- [10] Kalghatgi GT, Risberg P, Angstrom H-E. Advantages of Fuels with High Resistance to Auto-ignition in Late-injection. Low-temperature, Compression Ignition Combustion. *SAE Transactions* 2006;115:623–34.
- [11] Kalghatgi G, Hildingsson L, Johansson B. Low NOx and low smoke operation of a diesel engine using gasolinelike fuels. *J Eng Gas Turbines Power* 2010;132(9). doi: 10.1115/1.4000602.
- [12] Kalghatgi GT. The outlook for fuels for internal combustion engines: *Int. J Engine Res* 2014. <https://doi.org/10.1177/1468087414526189>.
- [13] Kalghatgi G, Johansson B. Gasoline compression ignition approach to efficient, clean and affordable future engines. *P I Mech Eng D-J Aut* 2018;232(1):118–38. <https://doi.org/10.1177/0954407017694275>.
- [14] Hildingsson L, Kalghatgi G, Tait N, Johansson B, Harrison A. Fuel octane effects in the partially premixed combustion regime in compression ignition engines. *SAE Technical Paper* 2019-01-2648 (2009). doi:10.4271/2009-01-2648.
- [15] Manente V, Johansson B, Cannella W. Gasoline partially premixed combustion, the future of internal combustion engines? *Int J Engine Res* 2011;12(3):194–208. <https://doi.org/10.1177/1468087411402441>.
- [16] Jiang C, Huang G, Liu G, Qian Y, Lu X. Optimizing gasoline compression ignition engine performance and emissions: Combined effects of exhaust gas recirculation and fuel octane number. *Appl Therm Eng* 2019;153:669–77. <https://doi.org/10.1016/j.applthermaleng.2019.03.054>.
- [17] Shankar V, Sajid MB, Al-Qurashi K, Atef N, Al Khesho I, Ahmed A, et al. Primary Reference Fuels (PRFs) as Surrogates for Low Sensitivity Gasoline Fuels, *SAE Technical Paper* 2016-01-0748 (2016). doi:10.4271/2016-01-0748.
- [18] Badra J, Viollet Y, Elwardany A, Im HG, Chang J. Physical and chemical effects of low octane gasoline fuels on compression ignition combustion. *Appl Energy* 2016; 183:1197–208. <https://doi.org/10.1016/j.apenergy.2016.09.060>.
- [19] Lopez JJ, Garcia-Oliver JM, Garcia A, Domenech V. Gasoline effects on spray characteristics, mixing and auto-ignition processes in a CI engine under Partially Premixed Combustion conditions. *Appl Therm Eng* 2014;70(1):996–1006. <https://doi.org/10.1016/j.applthermaleng.2014.06.027>.
- [20] Payri R, Garcia-Oliver JM, Xuan T, Bardi M. A study on diesel spray tip penetration and radial expansion under reacting conditions. *Appl Therm Eng* 2015;90:619–29. <https://doi.org/10.1016/j.applthermaleng.2015.07.042>.
- [21] Barths H, Hasse C, Peters N. Computational fluid dynamics modelling of non-premixed combustion in direct injection diesel engines. *Int J Engine Res* 2000;1(3): 249–67.
- [22] D'Errico G, Lucchini T, Contino F, Jangi M, Bai X-S. Comparison of well-mixed and multiple representative interactive flamelet approaches for diesel spray combustion modelling. *Combust Theory Model* 2014;18(1):65–88.
- [23] Pei Y, Hawkes ER, Kook S. Transported probability density function modelling of the vapour phase of an n-heptane jet at diesel engine conditions. *Proc Combust Inst* 2013;34(2):3039–47.
- [24] Mittal V, Cook DJ, Pitsch H. An extended multi-regime flamelet model for IC engines. *Combust Flame* 2012;159:2767–76.
- [25] Kong S-C, Han Z, Reitz RD. The Development and Application of a Diesel Ignition and Combustion Model for Multidimensional Engine Simulation. *SAE Trans* 1995; 104:502–18.
- [26] Colin O, Benkenida A. The 3-zones extended coherent flame model (ECFM3z) for computing premixed/diffusion combustion. *Oil Gas Sci Technol* 2004;59(6): 593–609.
- [27] Haworth DC. Progress in probability density function methods for turbulent reacting flows. *Prog Energy Combust Sci* 2010;36:168–259.
- [28] Felden A, Esclapez L, Riber E, Cuenot B, Wang H. Including real fuel chemistry in LES of turbulent spray combustion. *Combust Flame* 2018;193:397–416. <https://doi.org/10.1016/j.combustflame.2018.03.027>.
- [29] Lucchini T, D'Errico G, Cerri T, Onorati A, Hardy G. Experimental validation of combustion models for diesel engines based on tabulated kinetics in a wide range of operating conditions, *SAE Technical Paper* 2017-01-15 (2017).
- [30] Lucchini T, D'Errico G, Onorati A, Frassoldati A, Stagni A, Hardy G. Modeling non-premixed combustion using tabulated kinetics and different fame structure assumptions. *SAE Int J Engines* 2017;10(2):593–607.
- [31] Lionel M, Jean-Baptiste M, Stephane J, Olivier C. Evaluation of different tabulation techniques dedicated to the prediction of the combustion and pollutants emissions on a diesel engine with 3d cfd, *SAE Technical Paper* 2013-01-1093 (2015).
- [32] Naud B, Novella R, Pastor JM, Winklinger JF. RANS modelling of a lifted H₂/N₂ flame using an unsteady flamelet progress variable approach with presumed PDF. *Combust Flame* 2015;162:893–906.
- [33] Michel J-B, Colin O, Angelberger C, Veynante D. Using the tabulated diffusion flamelet model ADF-PCM to simulate a lifted methane air jet flame. *Combust Flame* 2009;156:1318–31.
- [34] Lucchini T, Pontoni D, D'Errico G, Somers B. Modeling diesel combustion with tabulated kinetics and different flame structure assumptions based on flamelet approach. *Int J Engine Res* 2020;21(1):89–100. <https://doi.org/10.1177/1468087419862945>.
- [35] Zhou Q, Lucchini T, D'Errico G, Maes N, Somers B, Lu Xc. Computational Modeling of Diesel Spray Combustion with Multiple Injections, *SAE Technical Paper* 2020-04-25 (2020). doi:10.4271/2020-01-1155.
- [36] Zhou Q, Lucchini T, D'Errico G, Hardy G. Validation of Diesel combustion models with turbulence chemistry interaction and detailed kinetics, *SAE Technical Paper* 2019-24-0088 (2019).
- [37] Zhou Q, Lucchini T, D'Errico G, Hardy G, Lu X. Modeling heavy-duty diesel engines using tabulated kinetics in a wide range of operating conditions. *Int J Engine Res* 2020. <https://doi.org/10.1177/1468087419896165>. 1468087419896165.
- [38] Engine Combustion Network — Engine Combustion Network Website. URL <http://ecn.sandia.gov/>.
- [39] Desantes JM, Garcia-Oliver JM, Xuan T, Vera-Tudela W. A study on tip penetration velocity and radial expansion of reacting diesel sprays with different fuels. *Fuel* 2017;207:323–35. <https://doi.org/10.1016/j.fuel.2017.06.108>.
- [40] Pastor JV, Garcia-Oliver JM, Lopez JJ, Vera-Tudela W. An experimental study of the effects of fuel properties on reactive spray evolution using Primary Reference Fuels. *Fuel* 2016;163:260–70. <https://doi.org/10.1016/j.fuel.2015.09.064>.
- [41] Singh S, Reitz RD, Musculus MPB. Comparison of the Characteristic Time (CTC), Representative Interactive Flamelet (RIF), and Direct Interaction with Detailed Chemistry Combustion Models against Optical Diagnostic Data for Multi-Mode Combustion in a Heavy-Duty DI Diesel Engine. *SAE Transactions* 2006;115:61–82.
- [42] Lehtiniemi H, Zhang Y, Rawat R, Mauss F. Efficient 3-D CFD Combustion Modeling with Transient Flamelet Models, *SAE Technical Paper* 2008-01-0957 (2008).
- [43] Peters N. Laminar diffusion flamelet models in non-premixed turbulent combustion. *Prog Energy Combust Sci* 1984;10(3):319–39. [https://doi.org/10.1016/0360-1285\(84\)90114-X](https://doi.org/10.1016/0360-1285(84)90114-X).
- [44] D'Errico G, Lucchini T, Onorati A, Hardy G. Computational fluid dynamics modeling of combustion in heavy-duty diesel engines. *Int J Engine Res* 2015;16(1): 112–24. <https://doi.org/10.1177/1468087414561276>.
- [45] Leung KM, Lindstedt RP, Jones WP. A simplified reaction mechanism for soot formation in nonpremixed flames. *Combust Flame* 1991;87(3):289–305. [https://doi.org/10.1016/0010-2180\(91\)90114-Q](https://doi.org/10.1016/0010-2180(91)90114-Q).
- [46] Payri R, Garcia-Oliver JM, Bardi M, Manin J. Fuel temperature influence on diesel sprays in inert and reacting conditions. *Appl Therm Eng* 2012;35:185–95. <https://doi.org/10.1016/j.applthermaleng.2011.10.027>.
- [47] D'Errico G, Lucchini T, Di Gioia R, Bonandrini G. Application of the CTC Model to Predict Combustion and Pollutant Emissions in a Common-Rail Diesel Engine Operating with Multiple Injections and High EGR, *SAE Technical Paper* 2012-01-0154 (2012).
- [48] Lucchini T, Cornolti L, Montenegro G, D'Errico G, Fiocco M, Teraji A, et al. A Comprehensive Model to Predict the Initial Stage of Combustion in SI Engines, *SAE Technical Paper* 2013-01-1087 (2013).
- [49] Lucchini T, Della Torre A, D'Errico G, Montenegro G, Fiocco M, Maghbouli A. Automatic Mesh Generation for CFD Simulations of Direct-Injection Engines, *SAE Technical Paper* 2015-01-0376 (2015). doi:10.4271/2015-01-0376.
- [50] Paredi D, Lucchini T, D'Errico G, Onorati A, Pickett L, Lacey J. CFD modeling of spray evolution for spark-ignition, direct injection engines. *AIP Conf Proc* 2019; 2191(1):020125. <https://doi.org/10.1063/1.5138858>.
- [51] Paredi D, Lucchini T, D'Errico G, Onorati A, Pickett L, Lacey J. Validation of a comprehensive computational fluid dynamics methodology to predict the direct injection process of gasoline sprays using Spray G experimental data. *Int J Engine Res* 2020;21(1):199–216. <https://doi.org/10.1177/1468087419868020>.
- [52] Ranzi E, Frassoldati A, Stagni A, Pelucchi M, Cuoci A, Faravelli T. Reduced Kinetic Schemes of Complex Reaction Systems: Fossil and Biomass-Derived Transportation Fuels. *Int J Chem Kinet* 2014;46(9):512–42. <https://doi.org/10.1002/kin.20867>.
- [53] Stagni A, Cuoci A, Frassoldati A, Faravelli T, Ranzi E. Lumping and Reduction of Detailed Kinetic Schemes: an Effective Coupling. *Ind Eng Chem Res* 2014;53(22): 9004–16. <https://doi.org/10.1021/ie403272f>.
- [54] Stagni A, Frassoldati A, Cuoci A, Faravelli T, Ranzi E. Skeletal mechanism reduction through species-targeted sensitivity analysis. *Combust Flame* 2016;163: 382–93. <https://doi.org/10.1016/j.combustflame.2015.10.013>.
- [55] Moiz AA, Ameen MM, Lee S-Y, Som S. Study of soot production for double injections of n-dodecane in CI engine-like conditions. *Combust Flame* 2016;173: 123–31. <https://doi.org/10.1016/j.combustflame.2016.08.005>.
- [56] Maes N, Bakker P, Dam N, Somers B. Transient Flame Development in a Constant-Volume Vessel Using a Split-Scheme Injection Strategy. *SAE Int J Fuels Lubr* 2017; 10(2):318–27. <https://doi.org/10.4271/2017-01-0815>.
- [57] Knox BW, Genzale CL, Pickett LM, Garcia-Oliver JM, Vera-Tudela W. Combustion Recession after End of Injection in Diesel Sprays. *SAE Int J Engines* 2015;8(2): 679–95. <https://doi.org/10.4271/2015-01-0797>.
- [58] Siebers DL, Higgins B. Flame Lift-Off on Direct-Injection Diesel Sprays Under Quiescent Conditions, no. 2001-01-0530, 2001. doi:10.4271/2001-01-0530.
- [59] Mizobuchi Y, Shinjo J, Ogawa S, Takeno T. A numerical study on the formation of diffusion flame islands in a turbulent hydrogen jet lifted flame. *Proc Combust Inst* 2005;30(1):611–9. <https://doi.org/10.1016/j.proci.2004.08.142>.
- [60] Yamashita H, Shimada M, Takeno T. A numerical study on flame stability at the transition point of jet diffusion flames. *Symp (Int) Combust* 1996;26(1):27–34. [https://doi.org/10.1016/S0082-0784\(96\)80196-2](https://doi.org/10.1016/S0082-0784(96)80196-2).
- [61] Jangi M, Lucchini T, Gong C, Bai X-S. Effects of fuel cetane number on the structure of diesel spray combustion: An accelerated Eulerian stochastic fields method. *Combust Theory Model* 2015;19(5):549–67. <https://doi.org/10.1080/13647830.2015.1057234>.
- [62] Pickett LM, Siebers DL. Soot Formation in Diesel Fuel Jets Near the Lift-Off Length: *Int. J Engine Res* 2006. <https://doi.org/10.1243/146808705X57793>.
- [63] Dec JE. A Conceptual Model of DI Diesel Combustion Based on Laser-Sheet Imaging. *SAE Trans* 1997;106:1319–48.
- [64] Derotte J, Dec JE, Ji C. Investigation of the Sources of Combustion Noise in HCCI Engines. *SAE Int J Engines* 2014;7(2):730–61. <https://doi.org/10.4271/2014-01-1272>.
- [65] Eng JA. Characterization of Pressure Waves in HCCI Combustion, *SAE Technical Paper* 2002-01-2859 (2002). doi:10.4271/2002-01-2859.